International Journal of Fracture, 2017.
ISSN: 0376-9429 (Print) 1573-2673 (Online)

Multi-scale analysis of the early damage mechanics of ferritized ductile iron

D. O. Fernandino[1*], A.P. Cisilino[1], S. Toro[2,3], P.J. Sanchez[2,3]

[1]*INTEMA, Universidad Nacional de Mar del Plata-CONICET, Av. Juan B Justo 4302, Mar del Plata, B7608FDQ, Argentina*

[2]*CIMEC-UNL-CONICET, Güemes 3450, CP 3000, Santa Fe, Argentina*

[3]*GIMNI-UTN-FRSF, Lavaise 610, CP 3000, Santa Fe, Argentina*

*Author E-mail: dfernandino@fi.mdp.edu.ar

Telephone/fax: +54 (223) 4816600 / +54 (223) 481-0046

Abstract

A multi-scale analysis of the linear elastic and the early damage stages of ferritic ductile iron is introduced in this work. The methodology combines numerical and experimental analyses in the macro and micro scales. Experiments in the micro-scale are used for the characterization of the material micro constituents and the assessment of the micro-scale damage mechanisms; experiments in the macro-scale provide the data to calibrate and validate the models. The 2D multi-scale problem is modeled using the pre-critical regime of the Failure–Oriented Multi-Scale Variational Formulation (FOMF), which is implemented via a FE^2 approach. Finite element analysis in the micro-scale is customized to account for plastic deformation and matrix-nodule debonding. The multi-scale model is found effective for capturing the sequence and extent of the damage mechanisms in the micro-scale and to estimate, via inverse analyses, parameters of the matrix-nodule debonding law. Results allow to develop new insights for the better understanding of the ductile iron damage mechanics and to draw conclusions related to the modeling aspects of the multi-scale simulation.

Keywords: *Ductile iron; fracture mechanisms; mechanical testing; multi-scale damage; finite elements.*

Abbreviations:

DI:	Ductile Iron.
FDI:	Ferritic Ductile Iron.
FTF:	First to Freeze zone.
LTF:	Last to Freeze zone.
RVE:	Representative Volume Element.
MNI:	Matrix-Nodule Interface.
MND:	Matrix-Nodule Decohesion.

International Journal of Fracture, 2017.
ISSN: 0376-9429 (Print) 1573-2673 (Online)

Notation

• Experimentally measured macro-scale quantities:

σ^{EXP}: stress.

ε^{EXP}: strain.

ε_p^{EXP}: plastic strain.

$\sigma_s^{EXP}, \varepsilon_s^{EXP}$: stress and strain at the MND process start.

$\sigma_e^{EXP}, \varepsilon_e^{EXP}$: stress and strain at the MND process end.

E_0^{EXP}: Young's modulus of the undamaged material.

E'^{EXP}: Young´s modulus as function of plastic strain.

$\sigma_{0,2}^{EXP}, \varepsilon_{0,2}^{EXP}$: offset yield stress and strain.

β^{EXP}: slope of the stress-strain curve in the elasto-plastic regime.

• Homogenized (effective) macro-scale quantities:

σ^{HOM}: stress.

ε^{HOM}: strain.

ε_p^{HOM}: plastic strain.

$\sigma_s^{HOM}, \varepsilon_s^{HOM}$: stress and strain at the MND process start.

$\sigma_e^{HOM}, \varepsilon_e^{HOM}$: stress and strain at the MND process end.

E_0^{HOM}: Young's modulus of the undamaged material.

E'^{HOM}: Young´s modulus as functions of plastic strain.

$\sigma_{0.2}^{HOM}, \varepsilon_{0.2}^{HOM}$: offset yield stress and strain.

β^{HOM}: slope of the stress-strain curve in the elasto-plastic regime.

• Micro-scale quantities are denoted with sub-indexes $(\cdot)_{\mu,i}$, where i indicates the micro-constituent phase, either the nodules (Nod), MNI, LTF or FTF.

$\boldsymbol{\sigma}_{\mu,i}$: micro-scale stress.

$\boldsymbol{\varepsilon}_{\mu,i}$: micro-scale strain.

$E_{\mu,i}$, $\nu_{\mu,i}$: elastic modulus and Poisson's ratio.

$\sigma_{\mu,i}^{y}$, $H_{\mu,i}$: yield stress and hardening modulus.

International Journal of Fracture, 2017.
ISSN: 0376-9429 (Print) 1573-2673 (Online)

1. Introduction

Ductile iron (DI) is a family of cast iron materials offering a wide range of properties obtained through microstructural control. As it is illustrated in Figure 1a, DI microstructure consists in a metallic matrix with a uniform random distribution of nearly-spherical graphite nodules. The matrix solidification structure consists of the "First To Freeze zones" (FTF), which are coincident with the axes and arms of the austenite dendrites, and the "Last To Freeze zones" (LTF), which result after the last portions of remaining melt between the solid phases (Tenaglia et al., 2016), see Figure 1b. DI mechanical properties are mainly determined by the metallic matrix; this is why they are identified as ferritic, pearlitic, martensitic, austempered, etc.

Ferritic DI (FDI) is commonly used when ductility, good impact properties and tensile and yield strengths equivalent to those of low carbon steel are specified. It can be produced "as cast", but annealing heat treatments can be used to enhance ductility and low temperature toughness. FDIs can achieve ultimate tensile strengths up to 440 MPa, yield strengths up to 289 MPa and maximum elongations between 12% and 20% (Ductile iron Data for Design Engineers, 2013).

Complementary to experimental work, computational mechanics emerges as a powerful tool to help to the better understanding of the effects of the microstructural features on the mechanical behavior of DI. The recent review paper by Hütter et al (2015a) provides a comprehensive overview and classification of the modeling strategies. The present work focuses on models with discrete microstructures, which can be grouped into two categories: micromechanical and homogenized multi-scale computational models. Their main features are summarily reviewed next.

Figure 1 Optical micrographs of FDI: (a) as-cast condition, (b) after annealing heat treatment and color etching

- *Micromechanical models*

Micromechanical models assimilate FDI to a heterogeneous material, whose macro-scale response is the result of the micro-scale constituent mechanical properties, morphology, quantity and size. Most of the works based on the micromechanical computational approach use Finite Element (FE) models of microstructural unit repetitive cells, i.e. they assume periodic microstructures with the nodules located at regular distances. The metal matrix is modeled as a homogeneous elasto-plastic material. In consideration to the "soft" nature of the graphite and the weak strength of the matrix-nodule interface (MNI), some works assimilate graphite nodules to voids.

For instance, this approach has been followed by Ghahremaninezhad and Ravi-Chandar (2012) and Hütter et al., (2015b) to investigate the onset and evolution of damage processes during the material deformation and failure. In contrast, Kuna and Sun (1996) concluded that to modelling graphite nodules as voids does not capture the nodule stiffening effect and, as consequence, the material lateral contraction is overestimated. Within this context, Bonora and Ruggiero (2005) and Andriollo et al. (2015, 2016) developed unit cell models in which nodules are assigned linear elastic and elasto-plastic behaviors, respectively. Models with

solid nodules use cohesive elements in order to account for the decohesion of graphite particles from the matrix and the initiation and propagation of cracks in the microstructure.

Although analyses based on periodic microstructures are suitable to elaborate qualitative descriptions of the material behavior, they may conduct to incorrect results, especially when non-linear phenomena are involved. This was shown by Kosteski et al. (2011), who used a discrete element method to model crack nucleation and coalescence for periodic and random nodule arrangements. Kosteski et al. (2011) showed that periodic nodule arrangements might conduct to premature and unrealistic rapid material collapses without strain localization. Other works based on random microstructures are due to Basso et al. (2009) and Ortiz et al. (2001). Basso et al. (2009) performed FE analysis with cohesive elements to show that the encapsulation of the LTF zones plays a key role as toughening mechanism; Ortiz et al. (2001) used boundary element models to assess the micromechanics of fatigue crack propagation in the near-threshold regime.

- *Homogenized multi-scale computational models*

Multi-scale computational models are based on the concepts of homogenization and representative volume elements (RVE). The RVE provides the description of the material at the micro-scale, while the homogenization transfers the information from the micro to the macro-scale. Thus, the material response at the macro-scale results after the material behavior in the micro-scale and the model adopted for the homogenization. A very valuable and comprehensive description, in terms of the mechanical backgrounds and the variational foundations of this approach, can be found in the contributions by de Souza Neto and Feijóo (2008, 2010) and Blanco et. al (2016a, 2016b). When complex heterogeneous materials are analyzed, the homogenization step is usually implemented through computational methods, such as in the FE^2 technique (Feyel et. al, 2000, 2003) The computational homogenization of the DI elastic response has been addressed by Boccardo et al. (2012), Carazo et al. (2014) and Fernandino et al. (2015). The paper by Fernandino et al. (2015) is a main antecedent for the present work. Fernandino et al. (2015) introduced a comprehensive methodology for the homogenization analysis that combines experimental and computational procedures: micrographic analyses and nano-indentation tests to retrieve the geometries and micro constituent properties for RVE models, and macroscopic tensile tests for the validation of the homogenization results. Among other results, Fernandino et al. (2015) concluded that RVEs obtained from 100× micrographs allow to compute homogenized Young's modulus and Poisson's ratios that differ less than 2% of the experimental values.

The extension of elastic homogenization analyses to the elasto-plastic regime and the subsequent fracture process is a highly complex task due to the numerous nonlinear phenomena in the micro-scale: matrix yielding and softening, nodule debonding and crack nucleation and propagation. Among others, matrix yielding and softening have been studied by Fritzen et. al (2012), Li and Steimann (2006) and Somer et al (2015), among others. Fritzen et. al (2012) and Li and Steimann (2006) performed multiscale analysis in which the micro-scale description considers only void distributions immersed in an elasto-plastic matrix, whereas Somer et al (2015) incorporated the effect of inclusion debonding due to the presence of weak interfaces between phase constituents. The synchronization of

numerical simulations of real microstructures with in-situ tensile tests are powerful tools to investigate the mechanisms of failure in metals, see for example Kadkhodapour et al (2011) and Matsumo et al (2015). In this sense, the recent work by Kasvayee et al. (2016) combine in-situ tensile testing, digital image correlation (DIC) and continuum FE models to study the microstructural deformation of a ferritic–pearlitic DI. Kasvayee et al. (2016) suggested that the introduction of cohesive elements can be used to model decohesion of graphite particles from the matrix. Thus, the FE simulations can be used to predict the structural strain that results in matrix-nodule decohesion.

As a first contribution towards the development of a multi-scale model that involves all DI failure phenomena, the present work concentrates in the analysis of the linear elastic and the early damage stages. The so-called early damage stage comprises the nodule debonding and distributed plasticity in the matrix, before plastic strain localization due to necking.

Figure 2 Experimental and computational multi-scale analysis methods. Mechanical quantities in the micro-scale are identified with the sub-index $(\cdot)_{\mu}$. Macro-scale quantities measured experimentally are identified with the supra-index $(\cdot)^{EXP}$, while those resulting from the computational homogenization procedure are denoted with the supra-index: $(\cdot)^{HOM}$

The methodology followed in this work is sketched in Figure 2. It combines experimental and multi-scale computational analyses:

a) *Experimental analyses*
   Experimental analyses encompass micro and macro-scale tests. The purpose of the micro-scale tests is twofold: the mechanical characterization of FDI micro-constituents via instrumented nanoindentation tests, and the monitoring of damage evolution via optical and scanning electron microscopy (SEM). In the macro-scale, standard tensile tests are used to measure the σ^{EXP} vs. ε^{EXP} curve, while unload-reload cycles are used to assess the microstructural damage through the analyses of the specimen stiffness reduction.

b) *Multi-scale computational analyses*
   Computational homogenization is performed using the pre-critical regime of the Failure–Oriented Multi-Scale Variational Formulation (FOMF) by Sanchez et al. (2013) and Toro et al. (2016a). The FOMF is implemented via the FE analysis of a RVE specifically designed for capturing plasticity and material damage mechanisms. Micro constituent phases are endowed with phenomenological constitutive models based on the experimental observations and tests. The FOMF correlates the intrinsic complexity of the microstructural damage process with the material macroscopic behavior to provide the homogenized σ^{HOM} vs. ε^{HOM} response. The macro-scale response does not assume any a-priori material constitutive behavior, i.e. no phenomenological plastic law is assumed at the macro-scale.

The remainder of this document is structured as follows: Section 2 introduces the macro and micro-scale material characterizations; Section 3 presents the formulation and implementation details of the multi-scale model; Section 4 is devoted to the results and discussion; finally, Section 5 presents the conclusions.

2. Experimental analyses

2.1 Ferritic Ductile Iron

One-inch "Y" blocks cast in sand molds provided by Megafund S.A were used as starting material. The annealing heat treatment consisted in an austenitizing at 900 ºC during 4 h, followed by a slow cooling down to room temperature inside the furnace. The chemical composition of the resulting FDI was determined by means of a Baird DV6 spectrometer. Results in Table 1 show that the FDI was slightly hypoeutectic.

Table 1

Chemical composition of ductile iron (weight %)

2.2 Macro-scale experiments

The macroscopic material response was assessed via tensile tests. Five small-size round tension test specimens (ASTM E8M-04) were machined from the Y-blocks and tested according to the specifications of the ASTM A897M-03. The experimental methodology was the same of that reported in Fernandino et al. (2015).

As it is sketched in Figure 2, the P (load) vs. Δ (displacement) data was used to retrieve the σ^{EXP} vs. ε^{EXP} response. The result is in Figure 3, where the error bars indicate the dispersion of the five tests. The initial value for the Young's modulus, E_0^{EXP}, and the offset yield stress and strain, $\sigma_{0.2}^{EXP}$ and $\varepsilon_{0.2}^{EXP}$, were computed from the σ^{EXP} vs. ε^{EXP} data using standard procedures. The hardening slope, β^{EXP}, was calculated as the best linear fit of the σ^{EXP} vs. ε^{EXP} data in the range $\varepsilon_{0.2}^{EXP} \leq \varepsilon^{EXP} \leq 1\%$, see Figure 3. The resultant values are E_0^{EXP}=172 ± 10 GPa, $\sigma_{0.2}^{EXP}$=275 ± 8 MPa, $\varepsilon_{0.2}^{EXP}$=0.35 ± 0.01 % and β^{EXP}=34 ± 3 MPa. It is emphasized that all measurements and calculations were made without assuming any a-priori material constitutive law.

Figure 3 Measured σ^{EXP} vs. ε^{EXP} curve: (a) complete deformation range up to failure, (b) details with the linear elastic and early damage stages. Error bars indicate the dispersion of the experimental results

Unloading-reloading tests were performed for three subsize rectangular tension test specimens at plastic strains ε_p^{EXP} = 0 %, 0.06 %, 0.15 %, 0.32 %, 0.49 % and 0.66 % and the corresponding elastic stiffness, E'^{EXP}, were measured , see

Figure **4**a. The results for the evolution of E'^{EXP}, in terms of the plastic strain, are reported through the quotient E'^{EXP}/E_0^{EXP} for each specimen in

Figure **4**b. Error bars indicate the dispersion for the three tests. Results in

Figure **4**b evidence the reduction of the material stiffness with plastic strain evolution, which is coherent with the undergoing damage process in the micro-scale due to the MNI debonding progress. This reduction is about 5% for ε_p^{EXP}=0.66%.

Specimens used for the unloading-reloading tests were polished for the monitoring of microstructural damage via micrographic analyses.

Figure 4 Experimental results for the unloading-reloading tests: (a) The σ^{EXP} vs. ε^{EXP} curve, (b) E'^{EXP}/E_0^{EXP} results. Error bars indicate the dispersion of the results

2.3 Micro-scale experiments

2.3.1 Micrographic observations

Metallographic samples were prepared using standard polishing and etching methods. Following the same methodology reported in Fernandino et al. (2015), a color reagent sensitive to microsegregation was used to reveal the FTF and LTF zones. Micrographs were obtained using an Olympus PMG3 optical microscope and digitally processed with Image Pro Plus software. Sample microstructures in the as-cast condition and after the annealing heat treatment are shown in Figure 1a and b, respectively. The as-cast characterization according to ASTM A247 resulted in a pearlitic microstructure with an average nodule size of 6 (which corresponds to a maximum nodules size of about 40 μm), nodularity higher than 95%, nodular count of 100 nodules/mm^2 and graphite area fraction of about 12%. Note the transformation of the fully pearlitic matrix in as-cast condition in Figure 1a to fully ferritic after the annealing heat treatment in Figure 1b. Note also the two different micro segregated zones, the FTF and LTF zones, reveled in Figure 1b.

SEM fractographic analyses were conducted on the broken specimens. Fracture path profiles were surveyed by optical microscopy following the procedure in Fernandino et al. (2015).

2.3.2 Failure mechanisms

Micrographic observations are correlated to the macroscopic σ^{EXP} vs. ε^{EXP} curves. Four stages are distinguished, see Figure 3:

i. The linear elastic stage, which encompasses macroscopic strains $\varepsilon^{EXP} \lesssim 0.1\%$. In the micro-scale, graphite nodules remain bonded to the matrix, as it has been observed by Bonora and Ruggiero (2005), Iacobiello et al. (2008), Di Cocco et al. (2014) and Fernandino (2015).

ii. The early damage stage, which involves the gradual Matrix-Nodule Decohesion (MND) and the localization of plastic strains that conduct to the formation of a plastic deformation band (PDB) across the matrix. As it is depicted in Figure 5, matrix-nodule decohesion was observed as a clean and neat separation of the MNI. However, it is worth to mention that there are reports of more complex decohesion mechanisms in which nodules fail with a "onion-like" pattern (Iacobiello et al., 2008; Di Cocco et al., 2010, 2014).

    The initiation of MND is shown in Figure 5a and Figure 5b for macroscopic strains $\varepsilon^{EXP} \cong 0.18\%$ and $\varepsilon^{EXP} \cong 0.35\%$, respectively. These observations are in agreement with those by Bonora and Ruggiero (2005) and Kasvayee et al., (2016), who also reported the onset of the MND before the macroscopic offset yield stress. The early damage stage encompasses macroscopic strains $\varepsilon^{EXP} \lesssim 1\%$.

iii. Ductile damage and crack nucleation. Once the MND is completed, the PDB is the driving mechanism for the development of ductile damage, see Di Cocco et al. (2010) and Kasvayee et al. (2016). Further load increments conduct to the nucleation of matrix cracks. Experimental observations show that nodular cavities in the matrix withstand high levels of distortion. Figure 5c and Figure 5d show highly-distorted nodular cavities that withstand $\varepsilon^{EXP} \cong 10\%$ and $\varepsilon^{EXP} \cong 18\%$. In addition, the first indication of cracks inside the matrix initiation is observed at approximately $\varepsilon^{EXP} \lesssim 3\%$. Crack nucleation is preferentially located at ferritic grain boundaries, LTF zones and inclusions, see Figure 6.

iv. Crack propagation and final fracture. Cracks propagate and they eventually coalesce into a single dominant crack that leads to the catastrophic material failure. The fracture surface exhibits a fully ductile fracture micromechanism with dimples and highly deformed nodule cavities. This is the failure mechanism usually reported for FDI under quasistatic loading conditions (see Di Cocco et al., 2014; Fernandino and Boeri, 2015; Ghahremaninezhad and Ravi-Chandar 2012; Kocatepe et al., 2007 and Martínez, 2010). As it is shown in Figure 7 nodules detach from the matrix while keeping their integrity. Note also in Figure 7a the high level of deformation of the nodular cavity.

Figure 5 Optical micrographs of matrix-nodule interfaces at different strain levels retrieved from the conical specimen: (a) $\varepsilon^{EXP} \cong 0.18\%$, (b) $\varepsilon^{EXP} \cong 0.35\%$, (c) $\varepsilon^{EXP} \cong 10\%$ and (d) $\varepsilon^{EXP} \cong 18\%$. Arrows in (a) and (b) indicate the localization of matrix-nodule debonding

Figure 6 Optical micrographs of matrix-crack initiation sites: (a) ferritic grain boundary, (b) LTF zone, and (c) inclusion. All three events are at $\varepsilon^{EXP} \cong 3\%$. Arrows indicate the localization of crack initiation

Figure 7 Detail of matrix-nodule interface after final fracture: (a) SEM and (b) optical micrographs

2.4 Micro-scale constituent characterization

The elastic characterization of nodules, FTF and LFT zones were performed via instrumented nano-indentation. Young's modules $E_{\mu,Nod}$, $E_{\mu,FTF}$ and $E_{\mu,LTF}$ were measured using the Oliver and Pharr method (Oliver and Pharr, 1992). Tests were practiced with a Tl900 Hysitron equipped with a multi-range nanoprobe and a Berkovich indenter. Load control method was used; maximum load was set at 9500 μN. In order to avoid interferences among the plastically deformed zones of adjacent imprints, indentations were separated at least three-times the imprint size. The results for the Young´s modules are summarized in Table 2. It is worth to note that the nodule Young´s modulus $E_{nod} = 15 \pm 4$ GPa is just below the threshold value of 20 GPa proposed by Andriollo et al. (2015, 2016).

The FTF and LTF plastic properties were assessed by means of inverse FE analyses of nano-indentation data for the force vs. displacement records, plastic zone sizes and pile-up heights. FTF and LTF were assumed to have elasto-plastic J2 responses with isotropic exponential hardening; they were described using the model by Simo and Hughes (2000). In that model, the yield surface is mainly characterized by the yield stress, while the strain hardening is described through the dependence of σ_μ^y with the cumulative equivalent plastic strain, α_μ, as follows:

$$\sigma_{\mu}^{y}(\alpha_{\mu}) = \sigma_{\mu}^{y,0} + H_{\mu}\alpha_{\mu} + \left(\sigma_{\mu}^{y,\infty} - \sigma_{\mu}^{y,0}\right)\left[1 - \mathrm{e}^{(-\delta_{\mu}\alpha_{\mu})}\right], \quad (1)$$

where $\sigma_{\mu}^{y,0}$ is the initial yield stress of the pristine material, $H_{\mu} \geq 0$ is the linear hardening modulus, and $\sigma_{\mu}^{y,\infty} \geq \sigma_{\mu}^{y,0} \geq 0$ and $\delta_{\mu} \geq 0$ are material parameters (see Appendix A for the details). A schematic representation of the elasto-plastic parameters in equation (1) is shown in Figure 8. The inverse analysis for the determination of σ_{μ}^{y}, H_{μ}, $\sigma_{\mu}^{y,\infty}$, $\sigma_{\mu}^{y,0}$ and δ_{μ}, for the FTF and LTF zones, was based in the method by Mata and Alcalá (2003), see Fernandino (2015) for the details. The results for the plastic properties are summarized in Table 2.

Figure 8 Schematic representation of the elasto-plastic parameters of the plastic model in equation (1)

Table 2

Material properties of the FDI micro-scale constituents.

3 Multi-scale modeling

The Failure Oriented Multi-Scale Formulation (FOMF) has been specifically developed to compute the effective macro-scale response of heterogeneous materials that undergo failure processes. It has the capabilities to nucleate cracks in the micro and the macro scales. The FOMF was proposed by Sanchez et al. (2013) and further developed by Toro et. al (2016a,b).

In the present work, the FOMF is used to model the linear elastic and early damage stages of FDI failure process (stages i and ii in Sections 2.3). During these stages, the limit criterion that triggers the macro-scale instability (i.e. the nucleation of a macro-crack) is not achieved, and therefore, the FMOF reduces to a classical multi-scale homogenization technique. Modelling the damage stages (iii) and (iv) requires of more elaborated and unconventional multi-scale formulations like in Belystchko et al. (2008), Nguyen et al. (2010) and Oliver et al. (2015).

The ingredients of the FOMF used in this work, and their customizations for the FDI analysis, are presented next.

3.1 Multi-scale formulation

We adopt the notation $(\cdot)^{HOM}$ to label the effective macro-scale magnitudes that result from the FOMF homogenization. For the present application, both macro and micro-scale problems are solved using the two-dimensional plane-strain hypothesis. Both, macro and micro-scale kinematics are assumed to comply with the infinitesimal strain theory. However, it is important to note that for the general formulation of the FOMF, the infinitesimal strain assumption in the macro-scale does not impose restrictions to strain magnitudes in the micro-scale.

The plane-strain hypothesis is a simplification of the actual three-dimensional FDI, microstructure which consists in a random distribution of nearly-spherical graphite nodules. However, there is evidence (see Rodríguez et al, 2015 and Kasvayee et al, 2016) that shows that, when restricted to the infinitesimal strain regime, the two-

dimensional simulations are effective to capture, identify and describe the relevant features of the phenomena occurring in the FDI micro-structure.

3.1.1 The classical multi-scale model for FDI

The "multi-scale constitutive model" is here understood as a constitutive relation at the macro-scale in the sense that, given a macro-scale strain, $\boldsymbol{\varepsilon}^{HOM}$, and after assuming some homogenization procedure, the multi-scale methodology provides the corresponding macro-scale stress, $\boldsymbol{\sigma}^{HOM}$. Figure 9 depicts this idea by means of a schematic layout of the model. Macro and micro-scale domains are denoted Ω and Ω_μ, respectively. The macro-scale domain coincides with the tensile specimen. In addition, at the macro-scale level of observation, the specimen is assumed to be constituted by a homogeneous material. The micro-scale domain Ω_μ is associated with the Representative Volume Element (RVE) of the FDI microstructure, which includes the FTF and LTF zones, the graphite nodules and the MNI (see Figure 1b). The macro-scale characteristic length L, say the specimen thickness, has order of centimeters while the micro-scale characteristic dimension l_μ has order of a tenth, or less, of a millimeter (say, the order of the nodule size). Under these circumstances, the scale separability requirement, $l_\mu \ll L$, is verified by two orders of magnitude.

Figure 9 Multi-scale approach of the traction test and RVE model

The boundary of Ω_μ is denoted Γ_μ, with normal outward vector $\boldsymbol{n}_\mu$. Coordinates $\boldsymbol{x}$ and $\boldsymbol{y}$ are related to reference systems in the macro and micro scales, respectively.

Recent approaches to RVE-based multi-scale models take advantages of the variational formalism; see for example Blanco et al. (2016a). In this context, "kinematics" and "virtual power" concepts play a fundamental role in the mechanical setting. Following such philosophy, a very fundamental definition introduced in this approach is the kinematically admissible requirement relating the macro-scale strain, ε^{HOM}, with the volumetric average of the micro-scale strain field, $\boldsymbol{\varepsilon}_\mu$. Specifically, it can be expressed as:

$$\boldsymbol{\varepsilon}^{HOM} = \frac{1}{|\Omega_\mu|}\int_{\Omega_\mu} \boldsymbol{\varepsilon}_\mu \, d\Omega_\mu \quad , \tag{2}$$

where $\boldsymbol{\varepsilon}_\mu$ is the strain observed at the micro-scale, i.e. at the RVE domain associated to the macroscopic position $\boldsymbol{x}$. The RVE volume is denoted $|\Omega_\mu|$.

Without loss of generality, the micro-scale strain, $\boldsymbol{\varepsilon}_\mu$, is defined as follows:

$$\boldsymbol{\varepsilon}_\mu = \boldsymbol{\varepsilon}^{HOM} + \tilde{\boldsymbol{\varepsilon}}_\mu, \tag{3}$$

so, the micro-strain consists of two parts: a constant value contributed by the macro-scale strain homogeneous insertion, $\boldsymbol{\varepsilon}^{HOM}$, and a fluctuating micro-scale strain, $\tilde{\boldsymbol{\varepsilon}}_\mu$, which varies within the RVE domain. Henceforth, the superimposed symbol $(\tilde{\cdot})_\mu$ is used to identify fluctuating fields at the RVE level.

Assuming linear kinematics hypothesis, the micro-scale strain fluctuation can be obtained as: $\tilde{\boldsymbol{\varepsilon}}_\mu = \nabla^s \tilde{\boldsymbol{u}}_\mu$, where $\tilde{\boldsymbol{u}}_\mu$ is the micro-scale displacement fluctuation

field and $\nabla^s(\cdot)$ stands for the symmetric gradient operator at the lower length scale. Note that the primary kinematical descriptor solved at the RVE level is $\widetilde{\boldsymbol{u}}_{\boldsymbol{\mu}}$.

Introducing the definition (3) into equation (2), it results:

$$\int_{\Omega_\mu} \tilde{\boldsymbol{\varepsilon}}_\mu \, d\Omega_\mu = \int_{\Omega_\mu} \nabla^s \widetilde{\boldsymbol{u}}_{\boldsymbol{\mu}} \, d\Omega_\mu = \int_{\Gamma_\mu} \widetilde{\boldsymbol{u}}_{\boldsymbol{\mu}} \otimes^s \boldsymbol{n}_\mu \, d\Omega_\mu = \mathbf{0} \,, \tag{4}$$

where the Green's theorem has been used to obtain the last boundary integral and the symbol $\otimes^s$ denotes the symmetric dyadic product. Equation (4) imposes a linear kinematical constraint on the field $\widetilde{\boldsymbol{u}}_{\boldsymbol{\mu}}$.

Only micro-scale displacement fluctuation fields satisfying (4) are kinematically admissible solutions for the mechanical problem at the RVE level. A widespread alternative adopted for describing the displacement fluctuations, which automatically fulfills the restriction (4), consists in enforcing periodic boundary conditions to $\widetilde{\boldsymbol{u}}_{\boldsymbol{\mu}}$ on Γ_μ. It is worth to mention that although the periodic boundary condition is rigorously valid for periodic microstructures, i.e. those composed by repeated unit cells in the domain, Terada el at (2000) showed that periodic boundary conditions could be applied to non-periodic heterogeneous media to get estimates of the mechanical properties. In fact, they showed that results obtained by means of other boundary conditions converge to the results obtained using periodic boundary conditions when the size of the sample is big enough. Therefore, this is the approach adopted in this work.

Next, we postulate the variational version of the Hill-Mandel principle of macro-homogeneity (Sánchez et al., 2013), which is enunciated as: the macro-scale internal virtual power density is equal to the volumetric average of the micro-scale internal virtual power density, for all kinematically admissible virtual actions. Taking into account (3) and (4), the variational Hill-Mandel principle can be formally expressed as:

$$\begin{gathered} \boldsymbol{\sigma}^{HOM} : \delta\boldsymbol{\varepsilon}^{HOM} = \frac{1}{|\Omega_\mu|} \int_{\Omega_\mu} \boldsymbol{\sigma}_\mu : \left(\delta\boldsymbol{\varepsilon}^{HOM} + \nabla^s \delta\widetilde{\boldsymbol{u}}_{\boldsymbol{\mu}} \right) d\Omega_\mu \,, \\ \forall\ \delta\boldsymbol{\varepsilon}^{HOM} \quad \text{and} \quad \forall\ \delta\widetilde{\boldsymbol{u}}_{\boldsymbol{\mu}} \quad \text{periodic in } \Gamma_\mu \,, \end{gathered} \tag{5}$$

where the stress observed at the micro-scale is denoted $\boldsymbol{\sigma}_\mu$ and the prefix $\delta(\cdot)$ identifies kinematically admissible virtual actions.

The variational sentence (5) is satisfied if the two subsequent conditions are enforced in the multi-scale formulation:

- The micro-scale stress field $\boldsymbol{\sigma}_\mu$ is self-equilibrated in the following variational sense:

$$\int_{\Omega_\mu} \boldsymbol{\sigma}_\mu : \left(\nabla^s \delta\widetilde{\boldsymbol{u}}_{\boldsymbol{\mu}} \right) d\Omega_\mu = \mathbf{0} \,, \qquad \forall\ \delta\widetilde{\boldsymbol{u}}_{\boldsymbol{\mu}} \text{ periodic in } \Gamma_\mu \,. \tag{6}$$

- The homogenized macro-scale stress is obtained through the homogenization rule:

$$\boldsymbol{\sigma}^{HOM} = \frac{1}{|\Omega_\mu|}\int_{\Omega_\mu} \boldsymbol{\sigma}_\mu \, d\Omega_\mu \, . \tag{7}$$

Expression (6) defines the micro-scale equilibrium problem in terms of $\tilde{\boldsymbol{u}}_{\boldsymbol{\mu}}$ (subjected to the linear kinematical constraint (4)), where the uniform insertion of the macro-scale strain $\boldsymbol{\varepsilon}^{HOM}$, into the RVE-domain, acts as a mechanical driving force.

Once computed the micro-scale stress field $\boldsymbol{\sigma}_\mu$ satisfying (6), the homogenized $\boldsymbol{\sigma}^{HOM}$ vs. $\boldsymbol{\varepsilon}^{HOM}$ response curve is obtained through the averaging formula (7). Homogenized material parameters can be extracted from that curves, as it will be shown later in Section 4.1.

3.1.2 Applicability limits for the proposed procedure.

Equations (2) to (7) describe the multi-scale homogenization procedure to model the pre-critical regime at the macro-scale (i.e. without macro-scale kinematical discontinuities such as cracks). This period includes the early damage stage of FDI we want to model. One of the higher limit of applicability of this procedure can be identify as the onset of macro-scale material instabilities, which corresponds to a critical condition on RVEs that experiment severe localized damage.

The criterion for detecting macro-scale instability is based on the spectral properties of the multi-scale homogenized constitutive tensor, $\mathbb{C}^{HOM}$, which is defined as:

$$\mathbb{C}^{HOM} = \frac{1}{|\Omega_\mu|}\int_{\Omega_\mu} \left(\mathbb{I} + \mathbb{A}_\mu\right) : \mathbb{C}_\mu^{tg} \, d\Omega_\mu, \tag{8}$$

where $\mathbb{I}$ is the fourth order identity tensor, $\mathbb{C}_\mu^{tg}$ is the micro-scale tangent constitutive tensor and $\mathbb{A}_\mu$ is the so-called localization tensor operator. The computation of $\mathbb{A}_\mu$ accounts for the effects of micro-scale fluctuation fields on $\mathbb{C}^{HOM}$. Typically, $\mathbb{A}_\mu$ is evaluated after solving a linear equilibrium problem, similar to (6), per each macro-scale strain canonical component (two pure stretching and a pure shear for the plane strain state), see Sanchez et al. (2013) for the details.

Given $\mathbb{C}^{HOM}$ from (8), we now introduce the concept of the homogenized acoustic tensor, $\boldsymbol{Q}^{HOM}$, as follows:

$$\boldsymbol{Q}^{HOM} = \boldsymbol{n} \cdot \mathbb{C}^{HOM} \cdot \boldsymbol{n} \ , \tag{9}$$

where $\boldsymbol{n}$ is an arbitrary unit vector defined at the macro-scale. Material stability, according with the FOMF criterion, is guaranteed whenever $\mathbb{Q}^{HOM}$ is positive definite for any vector $\boldsymbol{n}$:

$$det(\boldsymbol{Q}^{HOM}) > 0 \ , \ \forall \, \boldsymbol{n}. \tag{10}$$

Note that the criterion (10) is the classical strong ellipticity condition of the homogenized constitutive tangent tensor. The first time that $\boldsymbol{Q}^{HOM}$ becomes singular for some specific vector $\boldsymbol{n}^*$, i.e. $det(\boldsymbol{Q}^{HOM}) = 0$, indicates the critical

mechanical state at which, a continuous kinematical description at the macro-scale is no longer compatible. Material instability at the macro-scale might result in strain localization in small-width bands or crack nucleation in the direction perpendicular to vector $\boldsymbol{n}^*$.

Under these circumstances, the macro-scale stress-strain state losses homogeneity and the continuous multi-scale constitutive model in Section 3.1.1 is no longer valid. The condition (10) will be used in Section 4.1.2 to monitor the stability condition of early-damage stage simulations.

In addition to the macro-scale discontinuous bifurcation criterion, there are other limitations for the applicability of the present multiscale model that related to macro and micro strains magnitudes:

- The homogenized macro-scale strains should be compatible with the linear kinematic hypothesis.
- The sub-domains where micro-scale strains develop beyond the acceptable limit for infinitesimal strain theory have to be very spatially localized, such that its measure can be despicable compared with the whole RVE volume. If such a criterion is verified, the inaccuracies introduced during the stress homogenization process are negligible, because the error induced by adopting a "linear" kinematics at the micro-scale, has the order of the ratio between the volume of sub-domains with localized large strains and the entire RVE volume.

All the above conditions will be monitored throughout the numerical analyses (see in particular Sections 4.1.2 and 4.1.3) to guarantee the validity of the multiscale model.

3.2 Micro-cell finite element model for FDI micro-scale damage analysis

The problem at the micro-scale involves three material phases: the graphite nodules, the ferritic matrix, which includes the LTF and FTF zones, and the MNI (see Figure 9). Finite element meshes for the RVEs are illustrated in Figure 10b and Figure 9e. Meshes are generated from micrographs following the procedure introduced in Fernandino et al. (2015). Mechanical properties of the phases are modeled as follows:

- Graphite nodules are assumed linear elastic and homogenous. Elastic constants are the Young's modulus, $E_{\mu,Nod}$, and the Poisson's ratio, $\nu_{\mu,Nod}$, which were determined experimentally (see Table 2). Bi-lineal quadrilateral finite elements are used in the nodule discretization.
- The ferritic matrix is initially assumed as homogenous material (FTF zone properties). Then, the effect of incorporating the heterogeneous zones (LTF zones) in the macroscopic and microscopic response is reported in Section 4.3. In all cases, the ferritic matrix is modeled using the same phenomenological elasto-plastic J2 law adopted in Section 2.4 for its experimental characterization. Thus, expression (1) is specialized with the corresponding set of constants from Table 2 depending whether the FTF or LTF zones are considered. BBAR quadrilateral finite elements are used for the ferritic matrix (FTF and LTF zones). It is widely known that BBAR finite elements are adequate to deal with isochoric plastic strains.

- Matrix-nodule interfaces allow for the debonding mechanism between graphite nodules and the matrix. As it is shown in Figure 10c, MNI are modelled using thin band-like domains, denoted as cohesive bands, inserted between nodules and matrix. Cohesive bands are of finite thickness, and so, they can be endowed with a regularized continuum constitutive law, such as a conventional damage model with elastic stiffness degradation. The elastic stiffness degradation only develops under tensile stresses and its development produces the characteristic exponential strain softening effect, which is typically observed in damage models, see Figure 11.Therefore, cohesive-band domains can attain strain localization effects that might conduct to the mechanical separation between nodule and matrix. The details of the cohesive-band formulation can be found in Manzoli et al. (2012), Toro et al. (2016a, b) and Huespe et al. (2006).
  The damage constitutive law in Figure 11 is characterized by the Young's modulus, the Poisson's ratio, the critical stress, σ_{μ}^{c}, and the fracture energy, G_{μ}^{f}. The damage variable, d_{μ}, ranges from 0 to 1, where $d_{\mu} = 0$ indicates no damage and $d_{\mu} = 1$ indicates failure, this is, the complete loss of the element load-carrying capacity. Young's modulus and Poisson's ratio are assumed the same of the graphite nodules, $E_{\mu,MNI} = E_{\mu,Nod}$ and $\nu_{\mu,MNI} = \nu_{\mu,Nod}$. The values for σ_{μ}^{c} and G_{μ}^{f} could not be determined experimentally or found in the literature. So, they are left open for investigation in the next sections. The damage model formulation is summarized in Appendix B. Note that it naturally accounts for mixed mode fracture.

Figure 10 Finite element models at the micro-scale: (a) 100× micrograph, (b) Finite element mesh for a homogenous ferritic matrix (c) detail of the matrix-nodule interface, (d) 100× color-etched micrograph, (e) Finite element mesh for a heterogeneous ferritic matrix (FTF and LTF zones)

Figure 11 Constitutive law with degradation for the cohesive bands representing the MNI

Following Fernandino et al. (2015), an RVE taken from a 100× micrographs of size 530 µm x 397 µm and containing 32 nodules is used for the micro-scale simulations. Finite element discretization of the RVE consists of 10393 quadrilateral elements with average size of 5 µm and cohesive band thickness of about 0.04 µm. See Toro et al. (2016b) for additional details about the design of micro-cell finite element mesh.

3.3 Cases of analysis

The computational multi-scale analysis consists of four cases:

i) Characterization of the MNI damage parameters

As it was reported in the previous section, the MNI critical stress, σ_{μ}^{c}, and fracture energy, G_{μ}^{f}, are the only micro-scale material parameters that could not be experimentally measured. Therefore, we estimate their values via inverse analysis.

For the inverse analysis, a series of simulations for different combinations of σ_{μ}^{c} and G_{μ}^{f} are solved, and the pair $\left(\sigma_{\mu}^{c}, G_{\mu}^{f}\right)$ that results in the best agreement

between the simulation and the experimental data is identified. The series of multi-scale models combine increasing values of the critical stress $\sigma_\mu^c \geq$ 60 MPa with fracture energies in the range 250 N/m $\leq G_\mu^f \leq$ 10000 N/m. The limiting values for the fracture energies are those of the graphite nodules and to the FTF zones, respectively (graphite and FTF fracture energy data are from Basso et al., 2009). The comparison between the simulation results and the experimental data is done in terms of macro-scale σ vs. ε responses and the evolution of the damage mechanisms in the micro-scale. It is worth to note that the stress and strain fields of two-dimensional models are not the same of the actual three-dimensional problem. Therefore, we do not intend for thorough quantitative estimations of the parameter values. We seek for reasonable agreements between numerical and experimental results that allow drawing qualitative conclusions about the micro-scale damage mechanics.

Finally, two limiting cases are solved to help assess the effects of nodules: (a) a porous material for which the graphite nodules are assimilated to voids, and (b) a material with perfectly bonded nodules.

ii) Verification of the RVE size

It is worth to note that the RVE size here adopted is from the linear elastic analysis reported by Fernandino et al. (2015). Therefore, the suitability of the 100× RVE for the present non-linear damage case is verified. To this end, the independence of the multi-scale simulations is checked for larger micro-cell sizes.

iii) Influence of LTF zones

LTF zones are incorporated into the model to assess their influence on the material macro and micro-scale responses.

iv) Unloading-reloading cycles

Traction tests with unloading-reloading cycles are simulated in order to factorize the decrease of macro-scale elastic-stiffness by micro-scale internal fracture and heterogeneous yielding. Unloading-reloading cycles are performed at different macro-scale plastic strain values for the material with MND, the materials with pores and perfectly bonded nodules (see Case *i* above). Numerical results are analyzed and compared to the experimental results in Section 2.2.

4 Results

4.1 Characterization of the MNI damage parameters

4.1.1 Macroscopic response

Table 3 shows a summary of the micro-scale cohesive band property data (σ_μ^c and G_μ^f) and their corresponding homogenized macroscopic results in terms of the offset yield strength and strain, $\sigma_{0.2}^{HOM}$ and $\varepsilon_{0.2}^{HOM}$, and stress-strain slope β^{HOM} in the hardening regime. Values of $\sigma_\mu^c > 180$ MPa are not reported because systematically overestimate $\sigma_{0.2}^{HOM}$ and the post-yield stress level. Figure 12 and Figure 13 depict the σ^{HOM} vs. ε^{HOM} curves for the combinations of σ_μ^c and G_μ^f in

Table 3. In every case, the numerical results are compared to those of the experiments reported in Figure 3.

Consistently with the results in Fernandino et al. (2015), Figure 12 shows an excellent agreement between the experimental data and the numerical results for the linear regime. During this stage, numerical results are within the dispersion of the experiments, irrespectively of the MNI properties and the matrix plastic behavior. This result is coherent with the hypothesis that MNI remains bonded during the elastic regime, and so the linear response the macro-scale is associated with elastic responses of the micro-scale constituents.

The previous results are also consistent with those by Rodríguez et al (2015), who compared elastic properties of FDI computed by means of two- and three-dimensional homogenization analyses. Rodríguez et al (2015) found that the two sets of results differ in around 7%, which is of the same order of the dispersion of the experimental measurements of the Young´s modulus reported in Section 2.2. Thus, it might be argued that two-dimensional models provide results precise enough to capture the experimental behavior of the material in elastic regime.

Homogenized offset yield stresses in Table 3 are plotted in Figure 14a as a function of G_μ^f for different σ_μ^c. It can be observed that $\sigma_{0.2}^{HOM}$ mainly depends on σ_μ^c. The homogenized offset yield stress is underestimated for the lowest bound σ_μ^c=100 MPa, while it is overestimated for the upper bound σ_μ^c=180MPa. The best agreement between experiment, $\sigma_{0.2}^{EXP}$ =275 ± 8 MPa, and numerical results is in the range 120 < σ_μ^c < 140 MPa.

The interface fracture energy governs the post yield behavior. It can be observed in Figure 12a that the lowest value for the interface fracture energy, G_μ^f= 250 N/m, markedly underestimates the post-yield stress level, irrespectively of σ_μ^c. This behavior is assimilated to a premature debonding of the nodule-matrix interface. Note that the responses in Figure 12a are nearly identical to that for the porous material in Figure 13. As it is shown in Figure 12b to Figure 12d, higher G_μ^f values systematically increment the post-yield stress levels; the limiting case is that of the perfectly bonded nodules in Figure 13.

The homogenized post-yield results are compared to those of the experiments by means of the stress-strain slope coefficient, β^{HOM}, which is computed as the best linear fit of the stress vs. strain data in the range 0.5 % ≤ ε^{HOM} ≤ 1%. The results are reported in Table 3 and plot in Figure 14b.

Based on the previous analyses, it is concluded that G_μ^f= 5000 N/m and 120 < σ_μ^c < 140 MPa (shaded entries in Table 3) are the combination of MNI damage parameters that produces the best agreement between the simulation results and the experimental data; the simulation results for the offset yield stress and the strain-strain slope in the hardening regime are within the dispersion of the experimental data. The estimated values for G_μ^f and σ_μ^c are of the same order of those of the FTF (both are about half the corresponding values of the FTF-zone

damage properties) and, consistently to the background in Section 2.3.2, they confer the MNI a weaker fracture resistance than that of the FTF-zones. The comparison between the simulation results and the experimental observations in the microscale is done later in Section 4.1.3.

Table 3

Summary of the micro-scale cohesive band property data (σ_μ^c and G_μ^f) and their corresponding homogenized macroscopic results, $\sigma_{0.2}^{HOM}$, $\varepsilon_{0.2}^{HOM}$ and β^{HOM}. The experimental reference values are $\sigma_{0.2}^{EXP}$ =275 ± 8 MPa, $\varepsilon_{0.2}^{EXP}$= 0.35 ±0.01 % and β^{EXP}= 34 ± 3 MPa.

Figure 12 Homogenized macroscopic material responses for different combinations of the MNI fracture energies and critical stresses: (a) G_μ^f = 250 N/m, (b) G_μ^f = 2500 N/m, (c) G_μ^f = 5000 N/m and (d) G_μ^f = 10000 N/m. The black dashed lines are the experimental results; error bars indicate the experiment dispersion

Figure 13 Comparison between the experimental (black dashed line) and homogenized (symbols) σ vs. ε responses. Error bars indicate the dispersion of the experimental results

Figure 14 Results for (a) the homogenized offset yield strength: $\sigma_{0.2}^{HOM}$ and (b) slope coefficient of stress-strain curve at the hardening regime for the range 0.5 %< ε^{HOM}<1 %

4.1.2 Stability analysis

The stability of the homogenization procedure is verified by monitoring the condition in equation (10), which guarantees that no crack, or any other severe kinematical discontinuity, nucleates at the macro-scale. Figure 15 plots a typical evolution of the normalized acoustic tensor determinant, $det(\boldsymbol{Q}^{HOM})/E_{\mu,FTF}^2$, as functions of θ, the orientation angle of vector $\boldsymbol{n}$ with respect to the horizontal direction. To construct the plot, $det(\boldsymbol{Q}^{HOM})$ was evaluated for $-\pi/2 \leq \theta \leq \pi/2$ in increments of $\Delta\theta = 1.57\text{x}10^{-3}$. It can be observed that $det(\boldsymbol{Q}^{HOM})$ presents two minima. Minimum values progressively diminish as ε^{HOM} increases and, consequently, damage in the micro scale spreads. Curves labeled I to V correspond to the homologous strain levels in Figure 13. It can be observed that the condition $det(\boldsymbol{Q}^{HOM}) > 0$ is satisfied during the complete loading history up to the final deformation in correspondence with ε^{HOM}= 1%.
The conditions on the macro and micro strains magnitudes for the applicability of the multiscale analysis (see Section 3.1.2) will be assessed in the next.

Figure 15 Evolution of the normalized acoustic tensor determinant for the model with G_μ^f = 5000 N/m and σ_μ^c=140 MPa

4.1.3 Micro-scale response

Strain patterns and the MNI damage were monitored in the micro-scale to identify the homogenized stress and strain levels for which the MND and the PDB occur. The analyses were conducted for all the combinations of σ_μ^c and G_μ^f. Table 4 compiles the results for the macro-scale stress and strain associated to the MND start, σ_s^{HOM} and ε_s^{HOM}, and end, σ_e^{HOM} and ε_e^{HOM}. In every case, the stress and strain results are normalized with respect to $\sigma_{0.2}^{HOM}$ and $\varepsilon_{0.2}^{HOM}$, respectively, to facilitate their correlation with the macroscopic material behavior. It is observed that $\sigma_s^{HOM}/\sigma_{0.2}^{HOM}$ and $\varepsilon_s^{HOM}/\varepsilon_{0.2}^{HOM}$ primarily depend on σ_μ^c; both increase with σ_μ^c. The ratio $\sigma_s^{HOM}/\sigma_{0.2}^{HOM} < 1$ irrespectively of σ_μ^c, i.e. debonding always starts before the material evidences yielding in the macro-scale. On the other hand, debonding could finish either before or after yielding depending on σ_μ^c.

Debonding finalization is also influenced by the fracture energy, the larger G_μ^f the longer it takes the debonding to complete.

The simulations that resulted in the best agreement between homogenized and experimental results ($120 < \sigma_\mu^c < 140$ MPa and $G_\mu^f = 5000$ N/m, see Section 4.1.1) predict the MND onset at $\sigma_s^{HOM}/\sigma_{0.2}^{HOM} \cong 0.96$. This is, MND starts just before yielding, without appreciable influence of σ_μ^c. On the other hand, the strain level for the MND onset presents a larger dispersion, its average value is $\varepsilon_s^{HOM}/\varepsilon_{0.2}^{HOM} \cong 0.73$. In what respects to the MND finalization, it happens immediately after yielding at $\sigma_e^{HOM}/\sigma_{0.2}^{HOM} \cong 1.015$ and $\varepsilon_e^{HOM}/\varepsilon_{0.2}^{HOM} \cong 1.12$. As for the MND start, the strain value presents a larger dispersion than the stress one.

The above results allow to hypothesize that the MND in FDI is intimately related to the material yielding. Note that the main variation of $\sigma_{0.2}^{HOM}$ is obtained because of the variation in σ_μ^c, independently of the G_μ^f value (see Section 4.1.1).

Table 4

Stress and strain values for the matrix-nodule decohesion start and finalization.

Figure **16** illustrates the evolution of plastic strain and damage in the micro-scale for the simulation with σ_μ^c = 140 MPa and G_μ^f = 5000 N/m. The subfigures correspond to the strain levels labeled in Figure 13: (I) in the linear elastic regime, ε^{HOM}= 0.06%; (II) at the onset of the nonlinear macroscopic response, $\varepsilon^{HOM} \approx$ 0.16; (III) at the onset of nodule debonding, ε^{HOM} = 0.26%; (IV) after the full nodule debonding, $\varepsilon^{HOM} \approx$ 0.47% and (V) at ε^{HOM} =1%. Displacement fields in Figure **16** are magnified 2× to better show the deboned zones.

Figure **16**-I allows to observe that, despite the apparent macroscopic linear elastic response for this strain level, there are internodular ligaments that attain incipient plastic strains.

Figure **16**-II shows strain localization in the internodular zones forming the PDB, peak values of the equivalent plastic strain are around 1.2%. Note that the formation of PDB in the micro-scale reflects on the incipient loss of linearity in the macro-scale material response, see Figure 13.

Figure **16**-III depicts the onset of nodule debonding. Plastic strain in the PDB attains values of up to 2.5%. The above qualitatively agree with the experimental observations by Bonora and Ruggiero (2005), Di Cocco et al. (2010) and Kasvayee et al. (2016), who reported MND before macroscopic yielding. The PDB is clearly identifiable in

Figure **16**-IV; nodules are completely detached from the matrix.
Finally, Figure 16-V shows a marked increase in the plastic strain level in the PDB, and interesting finding is the partial MND for nodules outside the PDB.

Note that

Figure **16**-IV and

Figure **16**-V show high levels of plastic strain. However, the loci of these strains

levels are very localized. For a macroscopic strain ε^{HOM}= 1%, 95% of the plastified zone in the micro-scale model (see

Figure **16**-V) presents plastic strains less than 2%, whereas plastic strains less than 3% spread over 98% the plastified zone. It is argued that due to their high level of spatial localization, plastic strains that exceed the limit for the infinitesimal strain theory do not invalidate the multiscale model results.

The work by Kasvayee et al (2016) presents a very interesting result in what refers to three-dimensional effects – which are not assessed by the current two-dimensional model – on the PDBs. Kasvayee et al (2016) have observed that, despite the three-dimensional nature of the FDI microstructure, the locations of PDBs predicted by two-dimensional numerical simulations are identical to those experimentally measured by means of digital image correlation. The difference is in the values of the plastic strain, which was larger for the experiments. The results Kasvayee et al (2016) support the utilization of two-dimensional models to qualitatively capture the micro-scale patterns of the micro-scale plastic strain patterns of FDI.

Figure 16 Damage and plasticity evolution at the microstructural scale for the simulation with $\sigma_\mu^c = 140$ MPa and $G_\mu^f = 5.000$ N/m: (I) linear elastic regime, (II) onset of the nonlinear macroscopic response, (III) onset of the MND process, (IV) after the complete nodule debonding, and (V) at $\varepsilon^{HOM} = 1\%$. Displacement fields are magnified 2× to better show the deboned zones

Figure 17a and Figure 17b compare the simulation debonding pattern to an actual fracture path from the experiments. It is immediate to infer that the final fracture path results after the joining of the MNI debonded zones by means of cracks that propagate across the internodular ligaments in the PDB. Also note the prediction of MND outside the PDB (see Figure 17b), which is also observed in the micrograph in Figure 17c. Debonded interfaces outside the PDB are not part of the final failure path, but it might be argued their energy dissipation contributes to the overall material toughness. This phenomenon was reported by Ortiz et al. (2001) and Basso et al. (2009) for fatigue crack propagation in austempered ductile iron (ADI) and dual phase ADI, respectively.

Figure 17 Comparison of the fracture paths at the micro-scale: (a) 100× micrograph and (b) simulation result, (c) experimental evidence of debonding in a nodule outside the PDB

4.2 RVE size verification

Results presented in Sections 4.1 are outcomes of analyses performed using a single RVE geometry taken from a 100× micrograph. This criterion for the RVE sizing is based on the linear elastic analyses by Fernandino et al. (2015). The suitability of the 100×-RVE for the non-linear regime is verified next.

The simulation with σ_μ^c = 140 MPa and G_μ^f = 5000 N/m was performed four times using different 100×-RVEs and once using a 50×-RVE with 115 nodules. Figure 18 compares their homogenized stress vs. strain curves to that of the experiments. All numerical results lie within the dispersion of the experimental data. Results for 100×-RVEs exhibit a negligible dispersion. On the other hand, it is interesting to observe that 50×-RVE results in larger hardening slope than the 100×-RVEs. Results of the 50×-RVE were used to compute the offset yield stress, and the

stress and strain values for the MND start and end. The results are $\sigma_{0.2}^{HOM}$= 282 MPa, σ_s^{HOM} = 270 MPa, σ_e^{HOM} = 286 MPa, ε_s^{HOM} = 0.26% and ε_e^{HOM} = 0.40%.These results are almost coincident with those reported in Table 4 for the 100×-RVE. The maximum difference is for ε^{HOM} = 1%, where the σ^{HOM} by the 50×-RVE is 7% higher than that by the 100×-RVEs.

Based on the above results, it is concluded that 100× microstructural cell can be assimilated to an RVE for the analysis of the linear elastic and early damage stages. However, it will be necessary address the RVE sizing issue to model larger strain levels, say macroscopic strains $\varepsilon^{HOM} > 1\%$.

Figure 18 Comparison of the macroscopic stress vs. strain curves for RVE sizes 50× and 100× (four analysis cases). The black dashed line is the experimental data; error bars indicate the experiment dispersion

4.3 Influence of the LTF zones

LTF zones are incorporated into the models introduced in Section 4.2. Geometries of the LTF zones are taken from the micrographs, see Figure 10d-e. The model construction follows the procedure in Section 3.2; material properties for the LTF zones are given in Table 2.
Homogenized stress vs. strain responses of the simulations with the LTF zones are plotted in Figure 19, where they are also compared to the responses of the simulations without LTF zones and to the experimental results. It is observed that both sets of simulations lie within the dispersion of the experimental results.

Figure 19 Macroscopic stress vs. strain responses of models with and without considering LTF zones. The black dashed line is the experimental data; error bars indicate the experiment dispersion

The values for σ_s^{HOM}, σ_e^{HOM}, $\varepsilon_s^{HOM}$and ε_e^{HOM} that result from the simulations with the LTF zones are reported in Table 4; they are labeled as 140-LTF. It can be observed that the MND onset is not affected by the LTF zones, whereas the results for σ_e^{HOM} and ε_e^{HOM} in presence of the LTF zones are around 4% higher than those without the LTF zones. Based on these results, it is concluded that the LTF zones have not significant influence in the early damage stage. However, it is foreseen that LTF zones might play a key role on subsequent damage stages that involve higher levels of plastic strain and the nucleation and propagation of matrix cracks (Basso et al., 2009).

4.4 Unloading-reloading cycles

Figure **20** presents the results of the numerical simulation of the unloading-reloading cycles. The results are for the material with MNI characterized through the values σ_μ^c = 140 MPa and G_μ^f = 5000 N/m, and the two fictitious limiting cases presented in Section 3.3: the porous material for which the graphite nodules are assimilated to voids and the material with perfectly bonded nodules.

Unloadings were performed for the same plastic strain values of the experimental tests, see Section 2.2. Each simulation was performed using four different 100×-RVEs.

Figure **20**a depicts the σ^{HOM} vs. ε^{HOM} responses (to keep the plot clear, the response of a single RVE is shown for each material) together with the experimental curve as a reference.

Figure **20**b shows the evolution of the E'^{HOM} / E_0^{HOM} ratio as function of the macroscopic plastic strain for the three materials; numerical results are compared to the experimental values.

Figure **20**b shows that the porous and the perfectly bonded materials retain their initial stiffness for all the unloading-reloading cycles. These results allow us to conclude (as predictable) that micro-scale heterogeneous yielding is not the cause for the decrements of the macro-scale elastic-stiffness. On the other hand, the simulations for the material with MND exhibit the same behavior as the experimental results: the macro-scale elastic-stiffness progressively decreases with loading evolution. This result shows that macro-scale elastic-stiffness degradation is caused by the micro-scale MND progress. On average, numerical results tend to overestimate the elastic-stiffness decrement, but the dispersion of the numerical predictions overlaps that of the experiments. No attempt was made to calibrate the cohesive parameters to better reproduce the numerical results. Such a thorough quantitative analysis requires of a more detailed three-dimensional model to precisely represent the stress and strain distribution around the nodules. The agreement between numerical and experimental unloading-reloading tensile tests permits us to conclude that the material parameters related to the cohesive law proposed to the MNI (σ_μ^c and G_μ^f) have been satisfactorily inferred.

Figure 20 Results of the multiscale models for the traction tests with unloading-reloading cycles: (a) The σ^{HOM} vs. ε^{HOM} responses, (b) E'^{HOM}/E_0^{HOM} ratio at different macroscopic plastic strain values. Error bars indicate the dispersion of the results.

5 Conclusions

A two-dimensional multi-scale analysis of the linear elastic and the early damage stages of ferritic ductile iron has been presented. Numerical modelling is combined with experimental tests in micro and macro scales. Experiments at the micro-scale are used for the characterization of the material micro-scale constituents, while results of macro-scale experiments serve for the model calibration and validation.

The Failure-Oriented Multi-Scale Variational Formulation and its finite element implementation are effective to model the micromechanics of the early damage stage of FDI. The simulations capture the development of the plastic strain and the matrix-nodule debonding; numerical predictions for the evolution of the damage mechanisms agree with experimental observations. Despite the three-dimensional

nature of the FDI microstructure, the proposed two-dimensional multi-scale analysis produced a homogenized stress vs. strain response that matches the experimental results within the dispersion of the experimental data.

The main findings in what respects to FDI early damage mechanisms are:

- The formation of plastic deformation bands in the micro-scale reflects on the incipient linearity loss for the material response at the macro-scale. The pseudo yield stress in the macro-scale is associated to nodule-matrix debonding phenomena in the micro-scale.
- The nodule-matrix debonding can be described by a traction separation law that it is characterized in terms of the fracture energy, G_{μ}^{f}, and the critical stress, σ_{μ}^{c}. Since these parameters could not be measured via experiments, they were estimated by inverse numerical analysis. Estimated values, G_{μ}^{f} = 5000 N/m and critical stress $120 < \sigma_{\mu}^{c} < 140$ MPa, are of the same order of those of the FTF (both are about half the corresponding values of the FTF-zone damage properties) and, consistently to the experimental observation in the micro-scale, they confer the MNI a weaker fracture resistance than that of the FTF-zones.
- There is a decrement in the material macro-scale elastic-stiffness as consequence of the nodule-matrix interface decohesion. The decrease in the material elastic stiffness is around 5% for a macroscopic strain of around 0.65%.
- In concordance with the experimental evidence, the multi-scale model predicts the occurrence of nodule-matrix debonding for nodules outside the plastic deformation band. These debonded interfaces do not take part of the final failure path, but it might be argued that their energy dissipation contributes to the overall material toughness.
- The last-to-freeze zones do not have a strong influence on the mechanical behavior during the early damage stage, but it is foreseen that they might play a key role on the subsequent damage stages, which involve higher levels of plastic strain, nucleation and propagation of matrix cracks.
- It was observed from the experiments that matrix crack initiation takes place at a macroscopic strain of around 3%. Cracks initiate at ferritic grain boundaries, LTF zones and inclusions.

In what respects to the modeling aspects of the multi-scale simulation, the findings are:

- The early damage stage can be effectively modeled using infinitesimal strain formulations at the macro and micro scales. The modelling of the subsequent damage stages would require of a finite-strain formulation in the micro-scale to capture the strain localization within the plastic deformation band. In addition, the micro-scale will need to embed cohesive bands in the matrix discretization to capture the nucleation of the cracks that emanate from the debonded nodules.
- Micro-cell finite element models constructed from 100× micrographs and containing 32 nodules are representative volume elements for the two-dimensional analysis of the early damage stage. The modelling of the subsequent damage stages will require to address the representative-volume-

element sizing issue to account for the effects of last-to-freeze zones and finite strains.

- Further investigations using three-dimensional models are necessary to fully reproduce realistic stress triaxiality and plastic strains patterns at the microstructural scale; three-dimensional models will allow to attain thorough quantitative agreements between numerical simulations and experiments.

Acknowledgements

This research has been supported by grants awarded by CONICET (PIP 2013-2105 631), ANPYCT (PICT 2011-0159), the National University of Mar del Plata (ING 399-14) and the European Research Council under the European Union Seventh Framework Programme (FP/2007–2013) / ERC Grant Agreement N. 320815 (ERC Advanced Grant Project "Advanced tools for computational design of engineering materials" COMP-DES-MAT). The authors wish to express their gratitude to Prof. Alfredo Huespe (CIMEC-UNL-CONICET) for his valuable comments on the manuscript and for his assistance with the numerical simulations. The authors also acknowledge MEGAFUND S.A. for providing the material for the experimental analyses.

APPENDICES

In the following two appendices, subindices $(.)_\mu$, indicating that variables are defined at the micro-scale, have been removed to alleviate the notation.

APPENDIX A

Elasto-plastic model for the LTF and FTF matrix phases

The elasto-plastic model by Simo and Hughes (2000) is used for the matrix phases (LTF and FTF zones) at the micro-scale. The main equations governing this elasto-plastic model are presented in Box A and described next. The model parameters are identified in Figure 8.

Equation (A.1) is the additive decomposition of the strain tensor in its elastic, $\boldsymbol{\varepsilon}^e$ and plastic component $\boldsymbol{\varepsilon}^p$; equation (A.2) is the linear elastic relation between the elastic component of the strain and the stress tensor $\boldsymbol{\sigma}$. The evolution of the plastic strain is given by the flow rule (A.3), where the consistency parameter γ is the norm of the plastic strain rate. The function $g(\boldsymbol{\sigma}, \alpha)$ in equation (A.4) define the yield condition for $g = 0$. Equation (A.5) is the hardening law, which includes linear and exponential terms. The inequalities (A.7) describe the plastic loading / elastic unloading conditions.

BOX A: Elasto-plastic model with isotropic hardening

$$\boldsymbol{\varepsilon} = \boldsymbol{\varepsilon}^e + \boldsymbol{\varepsilon}^p \tag{A.1}$$

Elastic stress-strain relationships:

$$\boldsymbol{\sigma} = \mathbf{C}^e : (\boldsymbol{\varepsilon} - \boldsymbol{\varepsilon}^p) = \mathbf{C}^e : \boldsymbol{\varepsilon}^e \tag{A.2}$$

Flow rule:

$$\dot{\boldsymbol{\varepsilon}}^p = \gamma \boldsymbol{m} \quad ; \quad \boldsymbol{m} = \frac{\boldsymbol{\sigma}^{dev}}{|\boldsymbol{\sigma}^{dev}|} \quad ; \quad |\boldsymbol{m}| = 1 \tag{A.3}$$

Yield function and hardening law:

$$g(\boldsymbol{\sigma}, \mathrm{q}) = |\boldsymbol{\sigma}^{dev}| - \sqrt{\frac{2}{3}}\sigma^y(\alpha) \tag{A.4}$$

$$\sigma^y(\alpha) = \sigma^{y,0} + H\alpha + (\sigma^{y,\infty} - \sigma^{y,0})\left[1 - \mathrm{e}^{(-\alpha\delta)}\right] \tag{A.5}$$

$$\dot{\alpha} = \gamma \quad ; \quad \alpha(\dot{t} = 0) = 0 \tag{A.6}$$

Plastic loading / elastic unloading condition:

$$\gamma \geq 0 \;\; ; \; g \leq 0 \; ; \; \gamma g = 0 \tag{A.7}$$

Material parameters:

$\mathbf{C}^e$: Hooke Elasticity tensor (defined in terms of the Young's modulus E and the Poisson's ratio ν).

$\sigma^{y,0}$: initial yield stress, of the virgin state.
$\sigma^{y,\infty}$: saturation stress of the exponential hardening.
H: linear hardening modulus.
δ: exponential hardening coefficient.

APPENDIX B

Damage model of the cohesive bands modeling the MNI

The constitutive relation for the micro-scale bands, modeling the MNI, is described by the continuum damage law presented in Box B. This constitutive relation is from Simo and Ju (1987) and Oliver et al. (2002).

According with equation (B.1), the internal variables q and r determine the isotropic damage variable d, which defines the elastic stiffness degradation ruled by the elastic constitutive tensor $\mathbf{C}^e$. Initial values of r and q are r_0 and q_0, respectively (see equation (B.3)). The variable r can be seen as the maximum value of a strain norm reached during the loading history. The relation between r and q is given by the intrinsic softening modulus $\overline{H}^d$, as shown in equations (B.4). This parameter is depends on the fracture energy, G^f, and the critical stress, σ^c, see equation (B.5). The remarkable aspect of the damage model is the regularization of the intrinsic softening modulus, with the parameter k (the thickness of the cohesive band). The damage criterion (B.6) is defined in terms of the positive part of the effective stress, $\overline{\boldsymbol{\sigma}}^+$, such that damage evolves under tensile stress only.

BOX B: Isotropic continuum tensile-damage model

Elastic stress-strain relation:

$$\boldsymbol{\sigma} = (1-d)\,\mathbf{C}^e{:}\,\boldsymbol{\varepsilon} = \frac{q}{r}\underbrace{\mathbf{C}^e{:}\,\boldsymbol{\varepsilon}}_{\overline{\boldsymbol{\sigma}}} \quad ; \quad \overline{\boldsymbol{\sigma}}\text{: effective stress} \tag{B.1}$$

Damage variable:

$$d(r) = 1 - \frac{q}{r} \geq 0 \tag{B.2}$$

Strain-like internal variable:

$$r(t=0) = r_0 = \frac{\sigma^c}{\sqrt{E}} \tag{B.3}$$

Evolution law of the stress-like internal variable:

$$\dot{q} = k\overline{H}^d\dot{r} \quad ; \quad q \geq 0 \quad ; \quad q(t=0) = r_0 \tag{B.4}$$

$$\overline{H}^d(r) = -\frac{{r_0}^2}{G^f}\exp\left(-\frac{kr_0}{G^f}(r-r_0)\right) \; ; \; \overline{H}^d(r)\text{: softening modulus} \tag{B.5}$$

Damage criterion: (B.6)

$$g^d(\varepsilon, r) = \sqrt{\overline{\boldsymbol{\sigma}}^+ : \boldsymbol{\varepsilon}} - r \quad ; \quad \overline{\boldsymbol{\sigma}}^+ = \sum_{i=1}^{3} \langle \bar{\sigma}_i^+ \rangle \, \boldsymbol{e}_i \otimes \boldsymbol{e}_i$$

where:

$\overline{\boldsymbol{\sigma}}^+$: positive part of the microscopic effective stress

$\boldsymbol{e}_i$: principal direction of the tensor $\overline{\boldsymbol{\sigma}}^+$

$\langle \quad \rangle$: Mac Aulay brackets

$\bar{\sigma}_i^+ : i-$ th principal effective stress

Damage loading/ elastic unloading conditions:

$$\dot{r} \geq 0 \quad ; \quad g^d \leq 0 \quad ; \quad \dot{r} g^d = 0 \quad ; \tag{B.7}$$

Material parameters and symbols:

$\mathbf{C}^e$: Hooke Elasticity tensor (defined in terms of the Young's modulus E and the Poisson's ratio ν).

σ^c: critical stress.

G^f: fracture energy.

d: scalar damage variable.

r and q: strain-like and stress-like internal variables, respectively.

References

Andriollo T, Thorborg J, Hattel J (2015) The influence of the graphite mechanical properties on the constitutive response of a ferritic ductile cast iron- A micromechanical FE analysis. XIII International Conference on Computational Plasticity. Fundamentals and Applications COMPLAS XIII. 632-641

Andriollo T, Hattel J (2016) On the isotropic elastic constants of graphite nodules in ductile cast iron: Analytical and numerical micromechanical investigations. Mechanics of Materials 96:138–150. doi:org/10.1016/j.mechmat.2016.02.007

Basso A, Martinez R, Cisilino A, Sikora J (2009) Experimental and numerical assessment of fracture toughness of dual-phase austempered ductile iron. Fatigue and Fracture of Engineering Materials & Structures 33:1-11. doi:10.1111/j.1460-2695.2009.01408.x.

Belytschko T, Loehnert S, Song J (2008) Multi-scale aggregating discontinuities: A method for circumventing loss of material stability. International Journal for Numerical Methods in Egineering 73:869-894

Blanco P J, Sánchez P J, de Souza Neto E A, Feijóo R A (2016a) Variational foundations and generalized unified theory of RVE-based multi-scale models. Arch. Comput. Methods Eng. 23: 191–253

Blanco P J, Sánchez P J, de Souza Neto E A, Feijóo R A (2016b) The method of multiscale virtual power for the derivation of a second order mechanical model. Mechanics of Materials 99:53-67

Boccardo A D, Carazo F D, Giusti S M (2012) A comparison of effective properties of nodular cast-iron considering different shapes of the representative volume element. Mecánica Computacional, Volumen XXXI:1799-1819

Bonora N, Ruggiero A (2005) Micromechanical modeling of ductile cast iron incorporating damage. Part I: Ferritic ductile cast iron. International Journal of Solids and Structures 42:1401–1424. doi:10.1016/j.ijsolstr.2004.07.025

Carazo F D, Giusti S M, Boccardo D, Godoy L (2014) Effective properties of nodular cast-iron: A multi-scale computational approach. Computational Materials Science 82:378-390. doi:10.1016/j.commatsci.2013.09.044

de Souza Neto E A, Feijóo R A (2008) On the equivalence between spatial and material volume averaging of stress in large strain multi-scale solid constitutive models. Mechanics of materials 40, 10:803-811. doi:10.1016/j.mechmat.2008.04.006

de Souza Neto E A, Feijóo R A (2010) Variational foundations of multiscale consti- tutive models of solid: small and large strain kinematical formulation. In: de Souza Neto, E.A., Vaz, Jr., M., Muñoz Rojas, P. (Eds.), Computational Materials Modelling: From Classical to Multi-Scale Techniques. Wiley

Di Cocco V, Iacoviello F, Cavallini M (2010) Damaging micromechanisms characterization of a ferritic ductile cast iron. Engineering Fracture Mechanics 77:2016–2023. doi:10.1016/j.engfracmech.2010.03.037

Di Cocco V, Iacoviello F, Rossi A, Iacoviello D (2014) Macro and microscopical approach to the damaging micromechanisms analysis in a ferritic ductile cast iron. Theoretical and Applied Fracture Mechanics 69:26–33. doi:10.1016/j.tafmec.2013.11.003

Ductile Iron Data for Design Engineers (2013) Engineering Data. http://www.ductile.org/didata/Section3/3part1.htm. Accessed 23 January 2017

Fernandino D O, Cisilino A P, Boeri R E (2015) Determination of effective elastic properties of ferritic ductile cast iron by means computational homogenization and microindentation test. Mechanics of Materials 83:110-121. http://dx.doi.org/10.1016/j.mechmat.2015.01.002

Fernandino D O (2015) Fracture of ductile cast iron. Experimental analysis and multi-scale modelling. PhD Thesis. National University of Mar del Plata, March 2015. Mar del plata, Buenos Aires, Argentina.

Fernandino D O, Boeri R E (2015) Study of the fracture of ferritic ductile cast iron under different loading conditions. Fatigue Fract Engng Mater Struct. 38:610-620.

Feyel F, Chaboche J (2000) FE^2 multiscale approach for modelling the elastoviscoplastic behaviour of long fibre sic/ti composite materials. Computer Methods in Applied Mechanics and Engineering 183:309–330.

Feyel F (2003) A multilevel finite element method (FE^2) to describe the response of highly non-linear structures using generalized continua. Computer Methods in Applied Mechanics and Engineering 192:3233–3244.

Fritzen F, Forest S, Böhlke T, Kondo D, Kanit T (2012) Computational homogenization of elasto-plastic porous metals. International Journal of Plasticity 29:102-119.

Ghahremaninezhad A, Ravi-Chandar K (2012) Deformation and failure in nodular cast iron. Acta Materialia 60:2359–2368. doi:10.1016/j.actamat.2011.12.037

Huespe A, Oliver J, Pulido M, Blanco S, Linero D (2006) On the fracture models determined by the continuum-strong discontinuity approach. International Journal of Fracture, 137:211–229. doi:10.1007/s10704-005-3065-1

Hütter G, Zybell L, Kuna M (2015a) Micromechanisms of fracture in nodular cast iron: From experimental findings towards modeling strategies-A review. Engineering Fracture Mechanics 144:118–141. doi:10.1016/j.engfracmech.2015.06.042

Hütter G, Zybell L, Kuna M (2015b) Micromechanical modeling of crack propagation in nodular cast iron with competing ductile and cleavage failure. Engineering Fracture Mechanics 147:388–397. doi:10.1016/j.engfracmech.2015.06.039

Iacoviello F, Di Bartolomeo O, Di Cocco V, Piacente V (2008) Damaging micromechanisms in ferritic–pearlitic ductile cast irons. Materials Science and Engineering A 478:181–186

Kadkhodapour J, Butz A, Ziaei-Rad S, Schmauder S (2011) A micro mechanical study on failure initiation of dual phase steels under tension using single crystal plasticity model. International Journal of Plasticity 27:1103–1125. doi:10.1016/j.ijplas.2010.12.001

Kasvayee K A, Salomonsson K, Ghassemali E, Jarfors A E W (2016) Microstructural strain distribution in ductile iron; comparison between finite element simulation and digital image correlation measurements. Materials Science & Engineering A 655:27–35. doi:10.1016/j.msea.2015.12.056

Kocatepe K, Cerah M, Erdogan M (2007) The tensile fracture behaviour of intercritically annealed and quenched + tempered ferritic ductile iron with dual matrix structure. Materials and Design 28:172–181. doi:10.1016/j.matdes.2005.04.012

Kosteski L, Iturrioz I, Galiano Batista R (2011) The truss-like discrete element method in fracture and damage mechanics. International Journal for Computer-Aided Engineering and Software 28, 6:765-787. doi:10.1108/02644401111154664

Kuna M, Sun D Z (1996) Analyses of Void Growth and Coalescence in Cast Iron by Cell Models. Journal de Physique IV 6:113-122. doi:10.1051/jp4:1996611

Li Z H, Steinmann P (2006) RVE-based studies on the coupled effects of void size and void shape on yield behavior and void growth at micron scales. International Journal of Plasticity 22:1195–1216.

Manzoli O, Gamino A, Rodrigues E, Claro G (2012) Modeling of interfaces in two-dimensional problems using solid finite elements with high aspect ratio. Computers & Structures 94–95, 70–82. doi:10.1016/j.compstruc.2011.12.001

Martínez R A (2010) Fracture surfaces and the associated failure mechanisms in ductile iron with different matrices and load bearing. Engineering Fracture Mechanics 77:2749–2762. doi:10.1016/j.engfracmech.2010.07.013

Mata M, Alcala J (2003) Mechanical property evaluation through sharp indentations in elastoplastic and fully plastic contact regimes. J. Mater. Res. 17:1705-1709.

Matsuno T, Teodosiu C, Maeda D, Uenishi A (2015) Mesoscale simulation of the early evolution of ductile fracture in dual-phase steels. International Journal of Plasticity 74:17-34

Nguyen V P, Lloberas-Valls O, Sluys L J, Stroeven M (2010) Homogenization-based multi-scale crack modelling. Comput. Methods Appl. Mech. Eng. 200:1220–1236.

Oliver W C, Pharr G M (1992) An improved technique for determining hardness and elastic modulus using load and displacement sensing indentation experiments. Journal of Material Research 7, 6:1564-1583.

Oliver J, Huespe A E, Pulido M D G, Chaves E (2002) From continuum mechanics to fracture mechanics: the strong discontinuity approach. Engineering fracture mechanics 69,2:113-136.

Oliver J, Caicedo M, Roubin E, Huespe A E, Hernández J A (2015) Continuum approach to computational multi-scale modeling of propagating fracture. Comput. Methods Appl. Mech. Eng. 294:384–427.

Ortiz J, Cisilino A P, Otegui J L (2001) Boundary element analysis of fatigue crack propagation micromechanisms in austempered ductile iron. Engineering Analysis with Boundary Elements 25: 467-473.

Rodríguez F J, Dardati P M, Godoy L A, Celentano D J (2015) Evaluación de propiedades elásticas de la fundición nodular empleando micromecánica computacional. Rev. Int. Métodos Numér. Cálc. Diseño Ing. 31, 2: 91–105 (in Spanish).

Sánchez P J, Blanco P J, Huespe A E, Feijóo R A (2013) Failure-Oriented Multi-scale Variational Formulation: Micro-structures with nucleation and evolution of softening bands. Comput. Methods Appl. Mech. Engrg. 257: 221–247. doi:10.1016/j.cma.2012.11.016

Simo J C, Ju J W (1987) Strain- and stress-based continuum damage models—I. Formulation. International Journal of Solids and Structures 23, 7: 821-840.

Simo J C, Hughes T J R (2000) Computational Inelasticity. Springer-Verlag, New York, pp. 91-91.

Somer D, Peric D, de Souza Neto E A, Dettmer W G (2015) Yield surfaces of heterogeneous media with debonded inclusions. Engineering Computations 32, 6: 1802 -1813.

Terada K, Hori M, Kyoya T, Kikuchi N (2000). Simulation of the multiscale con-vergence in computational homogenization approaches. Int. J. Solids Struct. 37, 16:2285-2311.

Tenaglia N, Boeri R, Rivera G Massone J, 2016. International Journal of Cast Metals Research. 29, 1-2, 3, 112-120. doi: 10.1080/13640461.2015.1106783

Toro S, Sánchez P J, Blanco P J, de Souza Neto E A, Huespe A E, Feijóo R A (2016a) Multi-scale formulation for material failure accounting for cohesive cracks at the macro and micro scales. International Journal of Plasticity 76: 75-110. doi:10.1016/j.ijplas.2015.07.001

Toro S, Sánchez P J, Podestá J M, Blanco P J, Huespe A E, Feijóo R A (2016b) Cohesive surface model for fracture based on a two-scale formulation: computational implementation aspects. Comput. Mech. 58, 4: 549–585. doi: 10.1007/s00466-016-1306-y

Figure 1

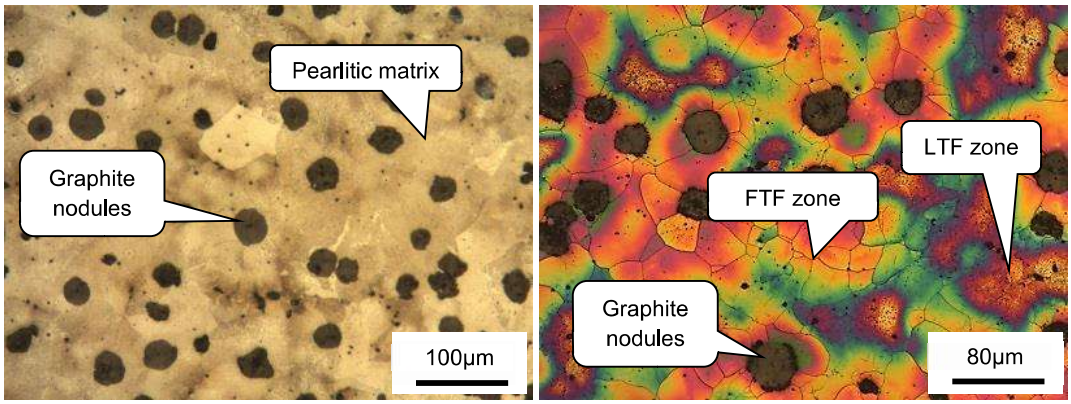
Pearlitic matrix
Graphite nodules
100μm
LTF zone
FTF zone
Graphite nodules
80μm

(a) (b)

Figure 2

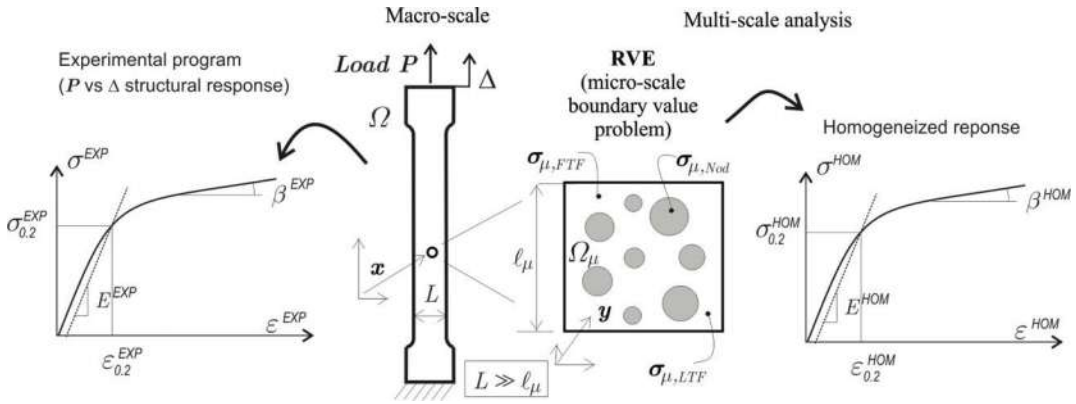
Macro-scale
Multi-scale analysis
Experimental program
(P vs Δ structural response)
Load P
Δ
Ω
RVE
(micro-scale
boundary value
problem)
Homogeneized reponse
σ^{EXP}
β^{EXP}
$\sigma^{EXP}_{0.2}$
E^{EXP}
ε^{EXP}
$\varepsilon^{EXP}_{0.2}$
$\boldsymbol{x}$
L
$\boldsymbol{\sigma}_{\mu,FTF}$
$\boldsymbol{\sigma}_{\mu,Nod}$
ℓ_μ
Ω_μ
$\boldsymbol{y}$
$\boldsymbol{\sigma}_{\mu,LTF}$
$L \gg \ell_\mu$
σ^{HOM}
β^{HOM}
$\sigma^{HOM}_{0.2}$
E^{HOM}
ε^{HOM}
$\varepsilon^{HOM}_{0.2}$

Figure 3

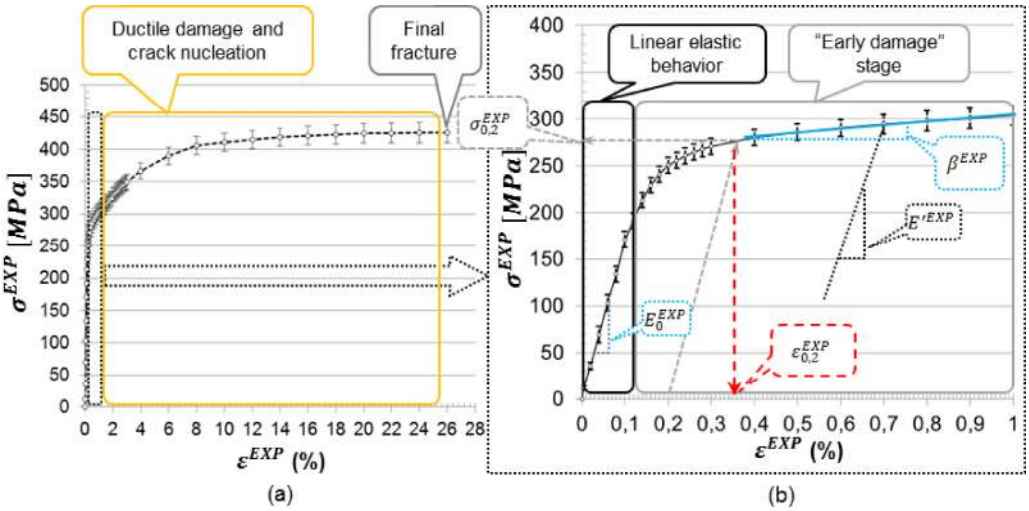
Ductile damage and crack nucleation
Final fracture
$\sigma_{0,2}^{EXP}$
σ^{EXP} [MPa]
ε^{EXP} (%)
(a)
Linear elastic behavior
"Early damage" stage
β^{EXP}
E'^{EXP}
E_0^{EXP}
$\varepsilon_{0,2}^{EXP}$
σ^{EXP} [MPa]
ε^{EXP} (%)
(b)

Figure 4

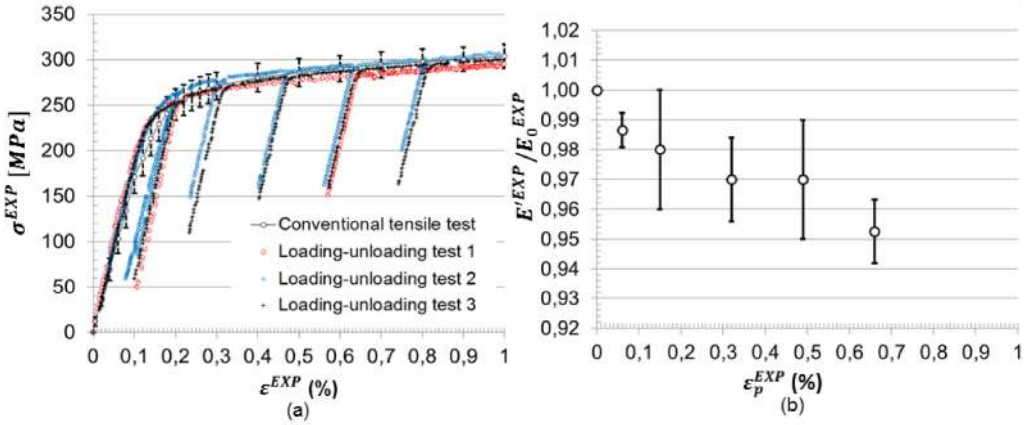
350
300
250
200
150
100
50
0
σ^{EXP} [MPa]
Conventional tensile test
Loading-unloading test 1
Loading-unloading test 2
Loading-unloading test 3
0 0,1 0,2 0,3 0,4 0,5 0,6 0,7 0,8 0,9 1
ε^{EXP} (%)
(a)
1,02
1,01
1,00
0,99
0,98
0,97
0,96
0,95
0,94
0,93
0,92
E'^{EXP}/E_0^{EXP}
0 0,1 0,2 0,3 0,4 0,5 0,6 0,7 0,8 0,9 1
ε_p^{EXP} (%)
(b)

Figure 5

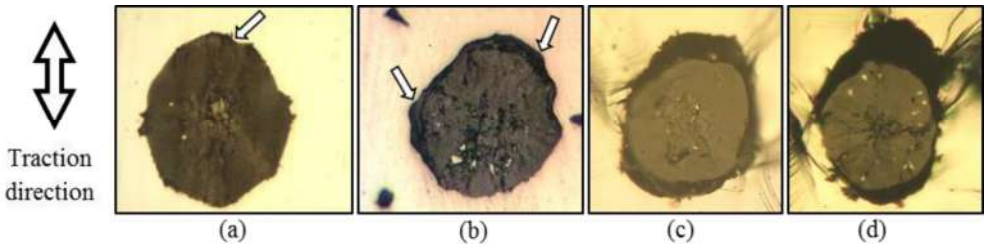

Figure 6

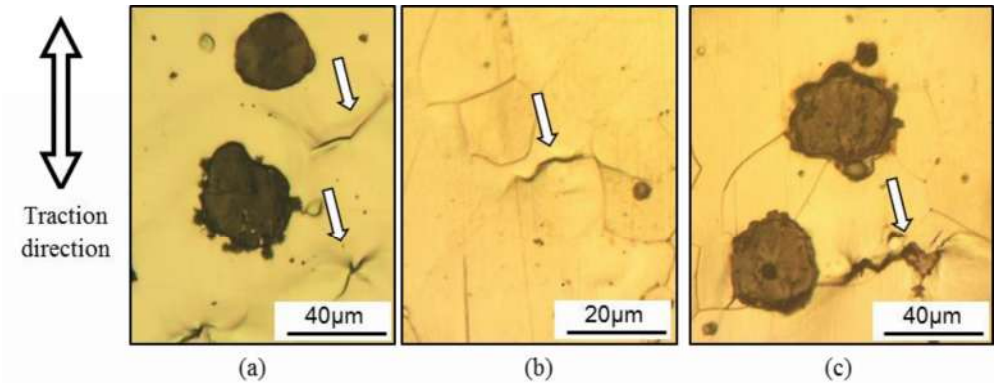

Figure 7

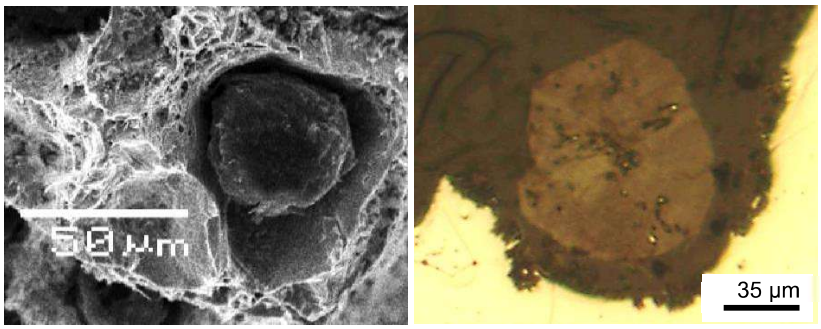

(a) (b)

Figure 8

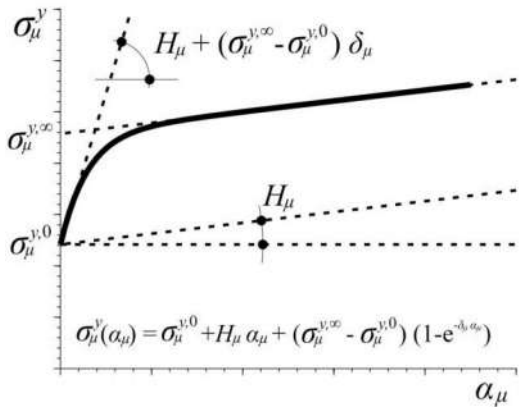
σ_μ^y
$H_\mu + (\sigma_\mu^{y,\infty} - \sigma_\mu^{y,0})\,\delta_\mu$
$\sigma_\mu^{y,\infty}$
H_μ
$\sigma_\mu^{y,0}$
$\sigma_\mu^y(\alpha_\mu) = \sigma_\mu^{y,0} + H_\mu\,\alpha_\mu + (\sigma_\mu^{y,\infty} - \sigma_\mu^{y,0})\,(1\text{-}e^{-\delta_\mu \alpha_\mu})$
α_μ

Figure 9

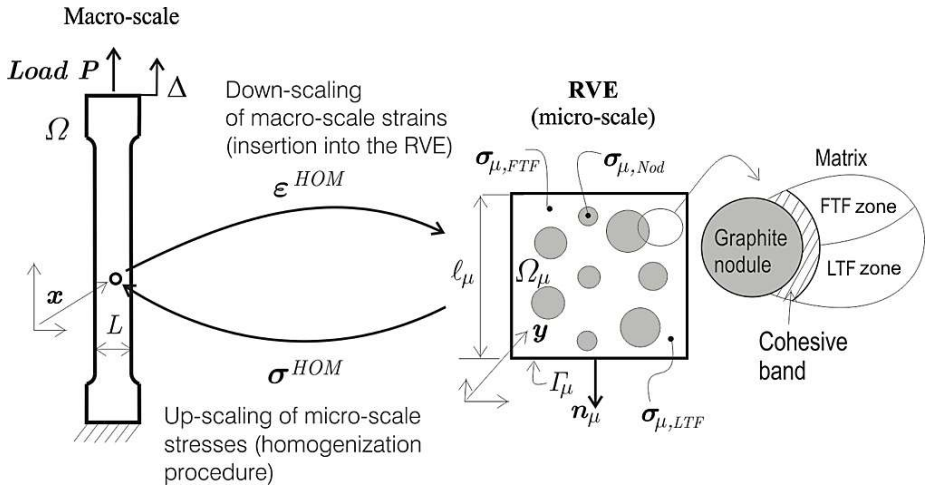
Macro-scale
Load P
Δ
Ω
x
L
Down-scaling
of macro-scale strains
(insertion into the RVE)
ε HOM
σ HOM
Up-scaling of micro-scale
stresses (homogenization
procedure)
RVE
(micro-scale)
σμ,FTF
σμ,Nod
ℓμ
Ωμ
y
Γμ
nμ
σμ,LTF
Matrix
FTF zone
Graphite
nodule
LTF zone
Cohesive
band

Figure 10

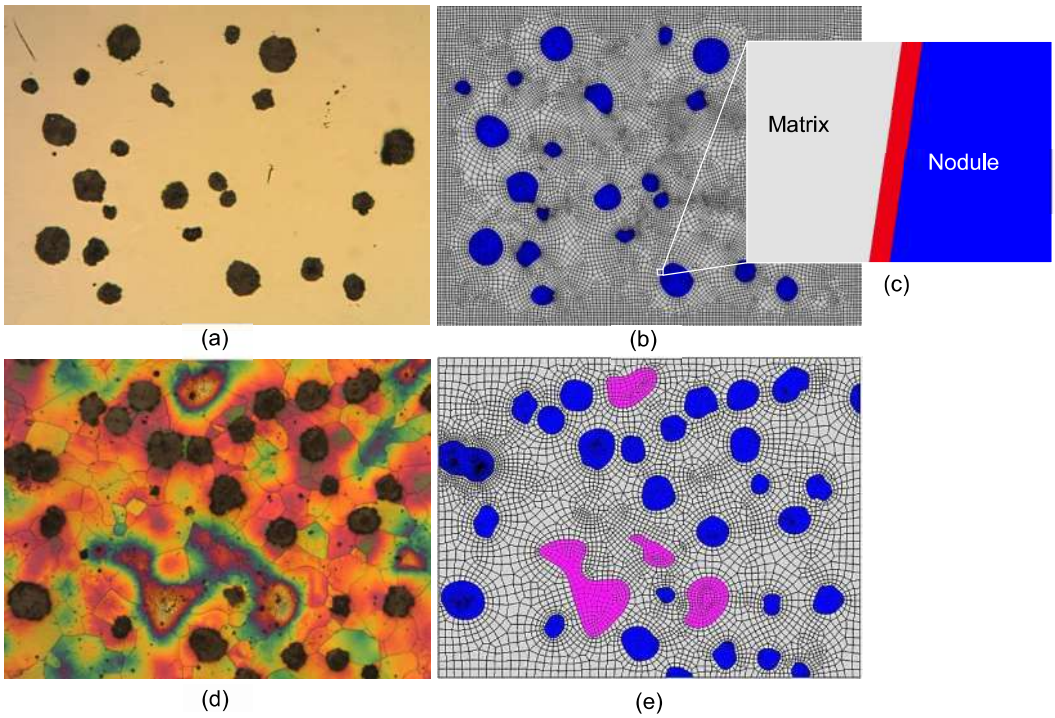

Figure 11

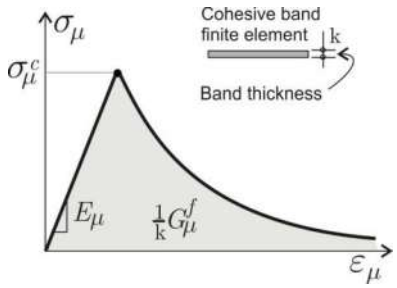

$0 \leq d_\mu \leq 1$

Figure 12

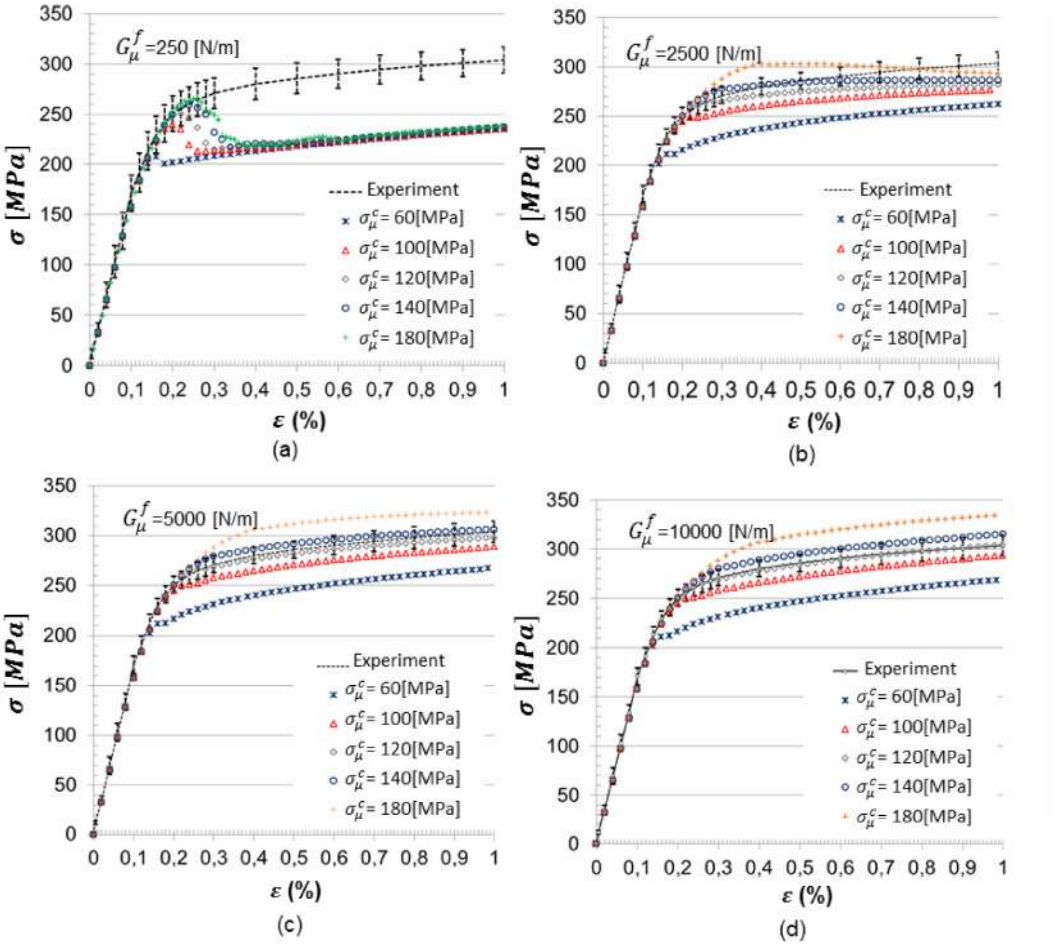
G_μ^f=250 [N/m]
G_μ^f=2500 [N/m]
G_μ^f=5000 [N/m]
G_μ^f=10000 [N/m]
Experiment
σ_μ^c= 60[MPa]
σ_μ^c= 100[MPa]
σ_μ^c= 120[MPa]
σ_μ^c= 140[MPa]
σ_μ^c= 180[MPa]
σ [MPa]
ε (%)
(a)
(b)
(c)
(d)

Figure 13

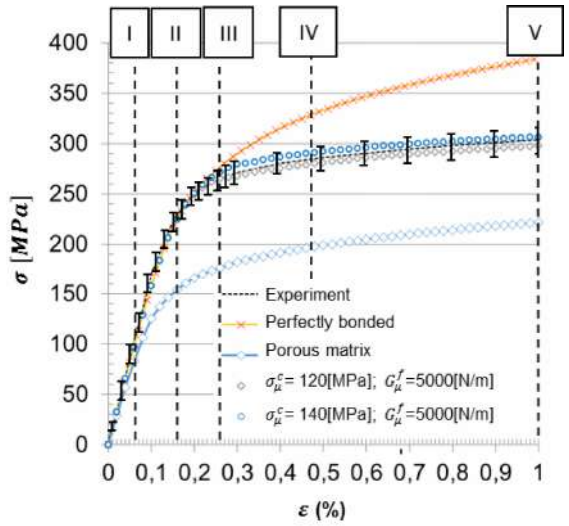
I
II
III
IV
V
400
350
300
250
200
150
100
50
0
0 0,1 0,2 0,3 0,4 0,5 0,6 0,7 0,8 0,9 1
σ [MPa]
ε (%)
Experiment
Perfectly bonded
Porous matrix
σ_μ^c= 120[MPa]; G_μ^f=5000[N/m]
σ_μ^c= 140[MPa]; G_μ^f=5000[N/m]

Figure 14

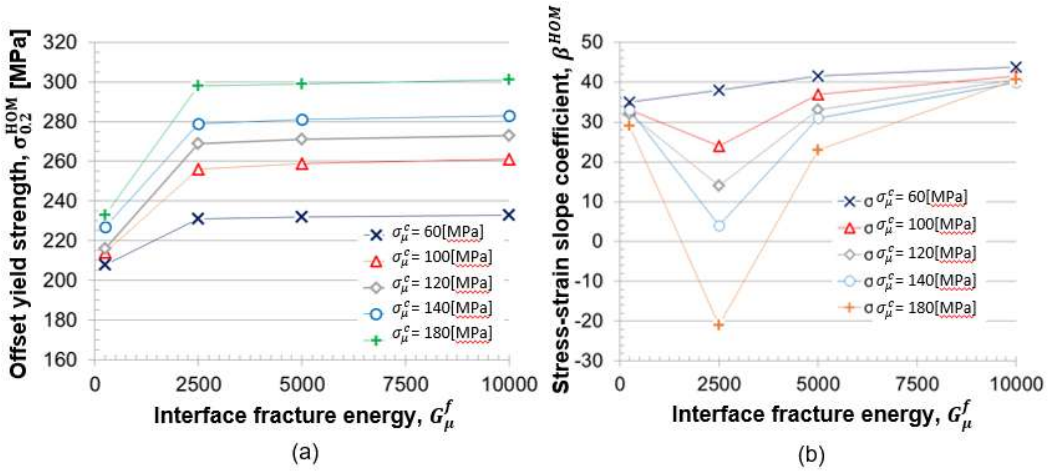
Offset yield strength, $\sigma_{0.2}^{HOM}$ [MPa]
320
300
280
260
240
220
200
180
160
0
2500
5000
7500
10000
Interface fracture energy, G_μ^f
σ_μ^c= 60[MPa]
σ_μ^c= 100[MPa]
σ_μ^c= 120[MPa]
σ_μ^c= 140[MPa]
σ_μ^c= 180[MPa]
(a)
Stress-strain slope coefficient, β^{HOM}
50
40
30
20
10
0
-10
-20
-30
0
2500
5000
7500
10000
Interface fracture energy, G_μ^f
σ_μ^c= 60[MPa]
σ_μ^c= 100[MPa]
σ_μ^c= 120[MPa]
σ_μ^c= 140[MPa]
σ_μ^c= 180[MPa]
(b)

Figure 15

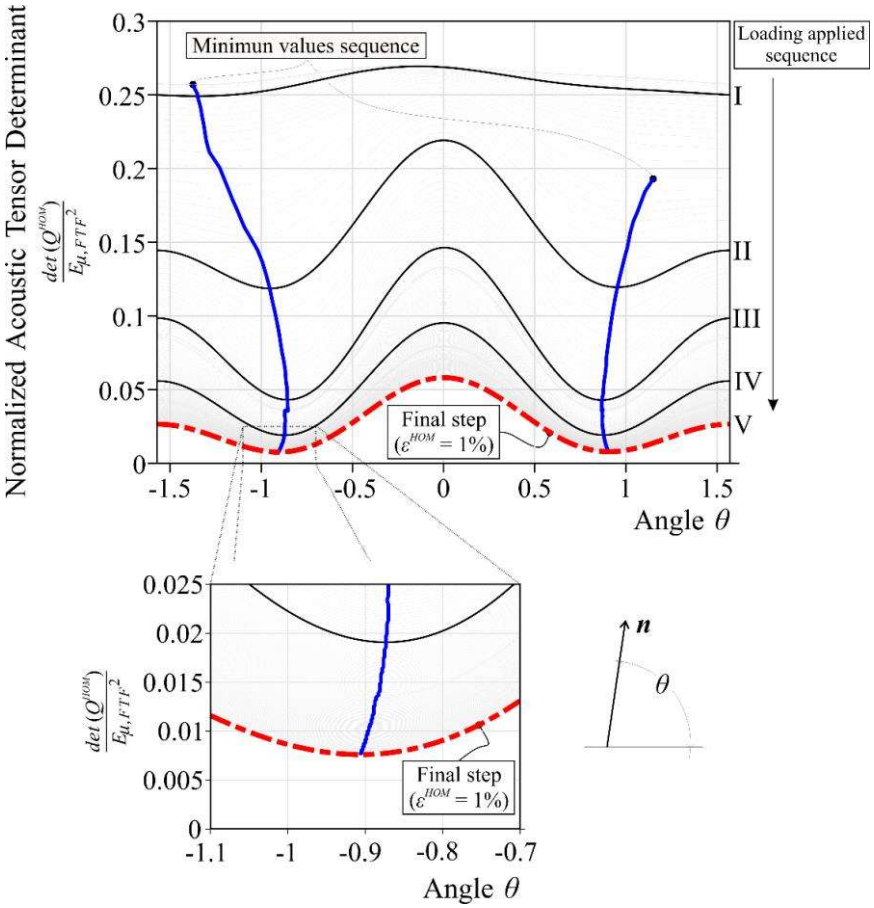
Normalized Acoustic Tensor Determinant
$\frac{det(Q^{HOM})}{E_{\mu,FTF}{}^2}$
Minimun values sequence
Loading applied sequence
I
II
III
IV
V
Final step
(ε^{HOM} = 1%)
Angle θ
n
θ

Figure 16

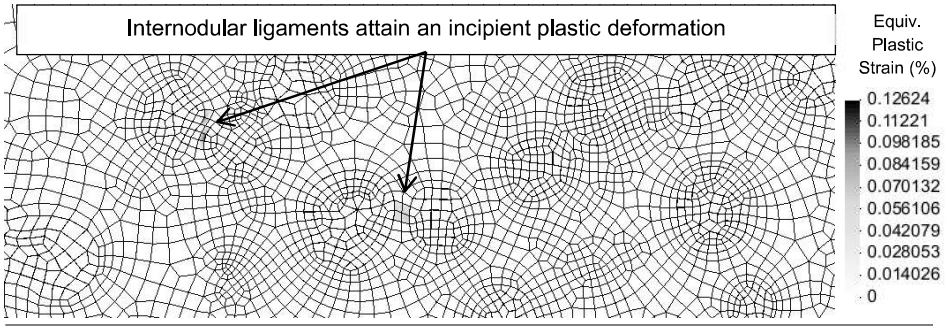

(I) σ^{HOM}=97[MPa]; ε^{HOM}=0.06%

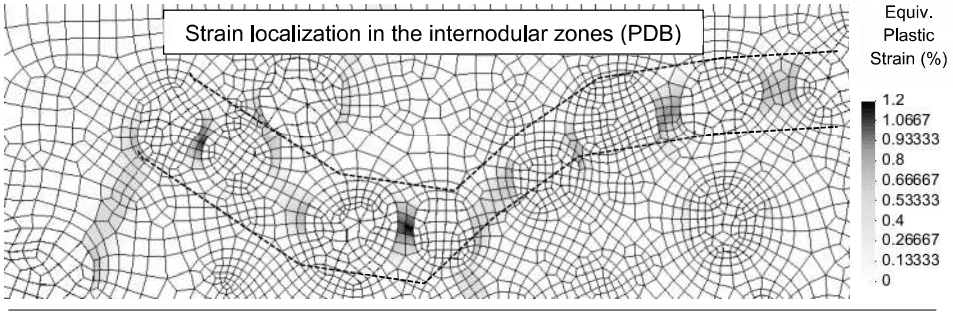

(II) σ^{HOM}=225[MPa]; ε^{HOM}=0.16%

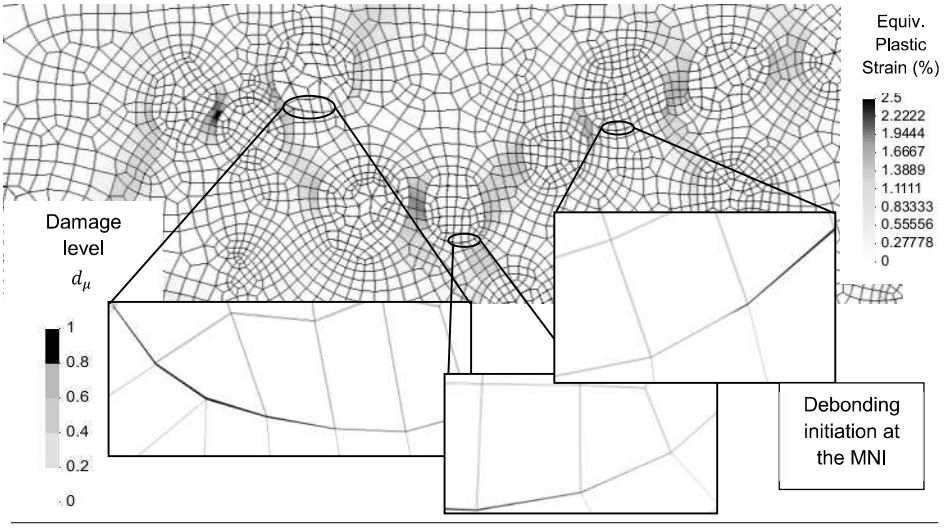

(III) σ^{HOM}=271[MPa]; ε^{HOM}=0.26%

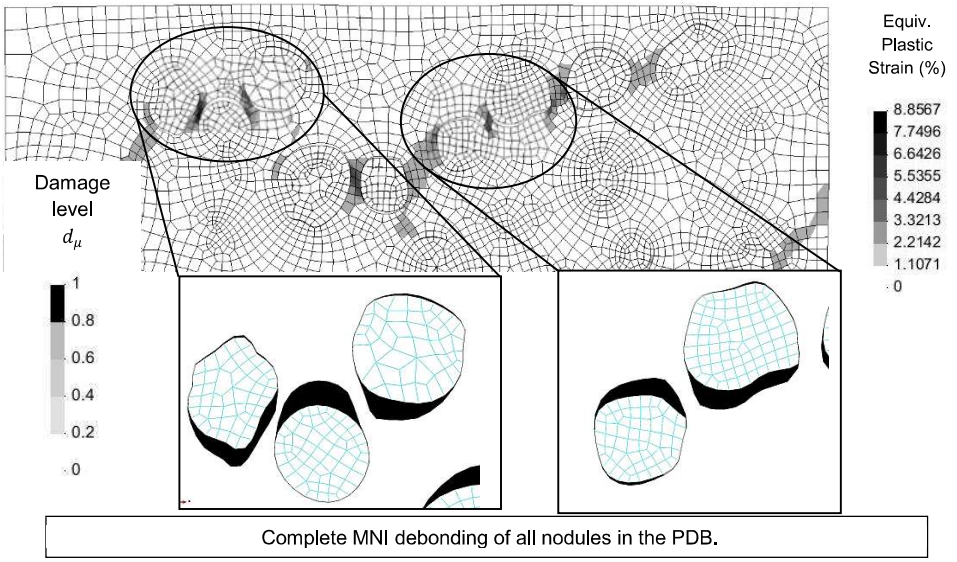

(IV) σ^{HOM}=290[MPa]; ε^{HOM}=0.47%

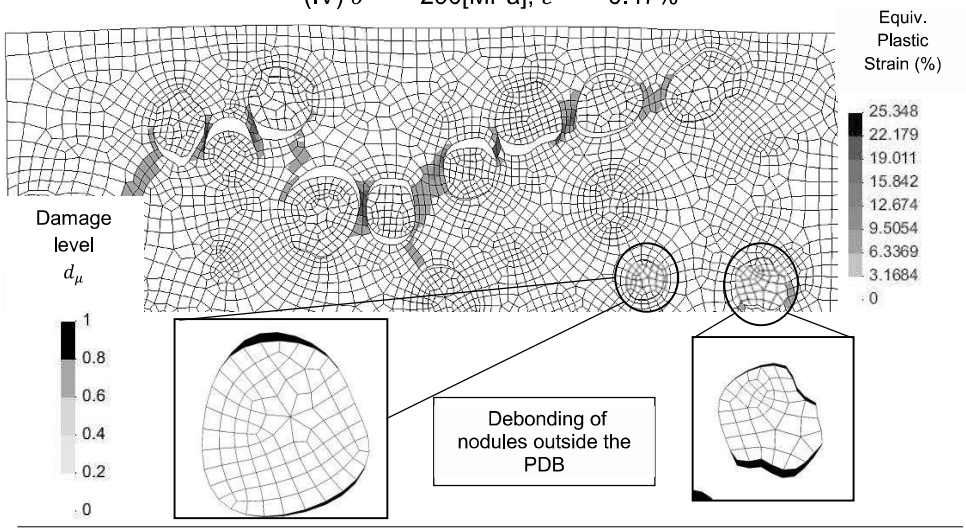

(V) σ^{HOM}=307[MPa]; ε^{HOM} =1%

Figure 17

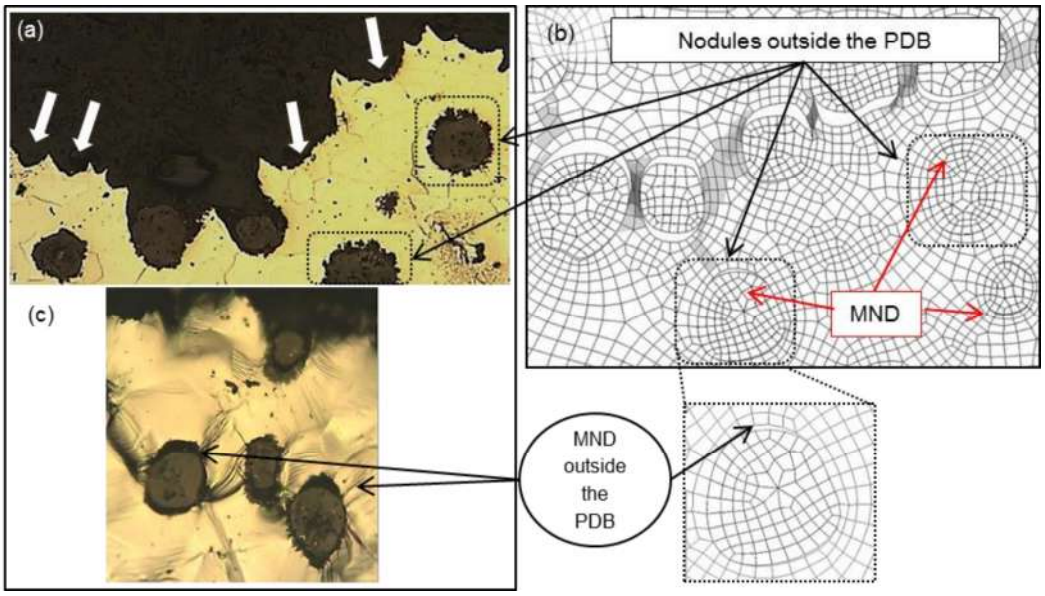

Figure 18

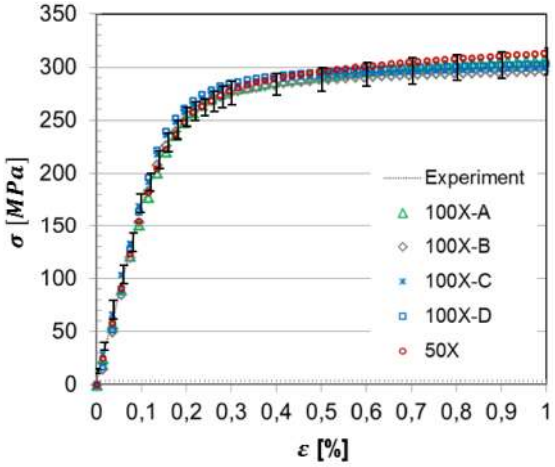
350
300
250
200
150
100
50
0
σ [MPa]
0 0,1 0,2 0,3 0,4 0,5 0,6 0,7 0,8 0,9 1
ε [%]
Experiment
100X-A
100X-B
100X-C
100X-D
50X

Figure 19

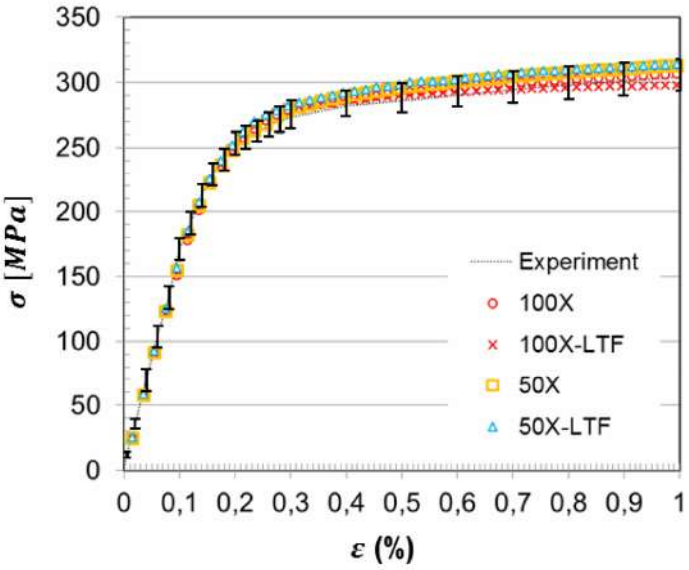
350
300
250
200
150
100
50
0
σ [MPa]
0
0,1
0,2
0,3
0,4
0,5
0,6
0,7
0,8
0,9
1
ε (%)
Experiment
100X
100X-LTF
50X
50X-LTF

Figure 20

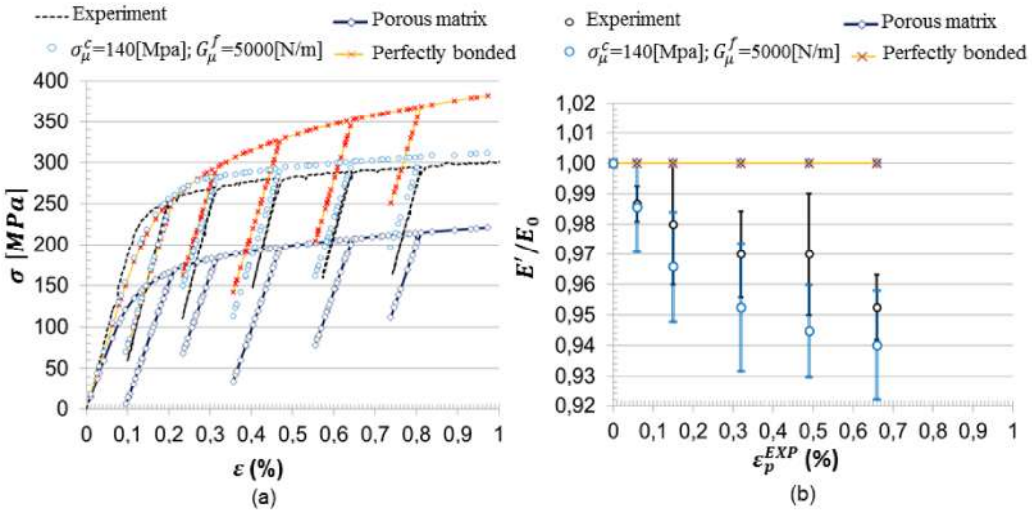
----- Experiment
Porous matrix
σ_μ^c=140[Mpa]; G_μ^f=5000[N/m]
Perfectly bonded
σ [MPa]
ε (%)
(a)
Experiment
Porous matrix
σ_μ^c=140[Mpa]; G_μ^f=5000[N/m]
Perfectly bonded
E'/E_0
ε_p^{EXP} (%)
(b)

Table 1

C	Si	Mg	Mn	Cu	Ni	S	P	Cr
3.32	2.36	0.03	0.31	0.62	0.02	<0.02	<0.02	0.05

Table 2

Constitutive model		Material constants					
		E_μ [GPa]	ν_μ	$\sigma_\mu^{y,0}$ [MPa]	$\sigma_\mu^{y,\infty}$ [MPa]	δ_μ	H_μ [MPa]
Nodule	Linear elasticity	15 ± 4	0.26	-	-	-	-
FTF	J2 elastoplasticity	212 ± 6	0.30	300± 15	540	20	180
LTF		239± 9	0.30	380± 18	710	20	260

Table 3

Multi-scale analysis cases					
Micro-scale Cohesive band properties		Homogenized macroscopic results			
σ_{μ}^{c}[MPa]	G_{μ}^{f} [N/m]	$\sigma_{0.2}^{HOM}$ [MPa]	$\sigma_{0.2}^{HOM}/\sigma_{\mu}^{c}$	$\varepsilon_{0.2}^{HOM}$ [%]	β^{HOM}[MPa]
60	250	208	3.47	0.301	35
	2500	231	3.85	0.309	38
	5000	232	3.87	0.309	42
	10000	233	3.88	0.315	44
100	250	214	2.14	0.306	33
	2500	256	2.56	0.325	24
	5000	259	2.59	0.327	37
	10000	261	2.61	0.333	42
120	250	216	1.8	0.307	32
	2500	269	2.24	0.332	14
	5000	271	2.26	0.334	34
	10000	273	2.28	0,340	41
140	250	227	1.62	0.313	33
	2500	279	1.99	0.339	4
	5000	281	2.01	0.340	31
	10000	283	2.02	0.347	40
180	250	233	1.29	0.318	29
	2500	298	1.66	0.351	21
	5000	299	1.66	0.350	23
	10000	301	1.67	0,359	41
Perfectly bonded nodules		296	-	0,356	100
Porous material		179	-	0,278	46

Table 4

σ_μ^c [MPa]	G_μ^f [N/m]	Nodule debonding start				Nodule debonding end			
		σ_s^{HOM} [MPa]	$\sigma_s^{HOM}/\sigma_{0,2}^{HOM}$	ε_s^{HOM} [%]	$\varepsilon_s^{HOM}/\varepsilon_{0,2}^{HOM}$	σ_e^{HOM} [MPa]	$\sigma_e^{HOM}/\sigma_{0,2}^{HOM}$	ε_e^{HOM} [%]	$\varepsilon_e^{HOM}/\varepsilon_{0,2}^{HOM}$
60	2500	182	0.79	0.12	0.39	211	0.91	0.18	0.57
	5000	193	0.83	0.13	0.42	216	0.93	0.20	0.65
	10000	197	0.85	0.14	0.43	218	0.94	0.21	0.67
100	2500	233	0.91	0.18	0.54	253	0.99	0.29	0.88
	5000	234	0.90	0.18	0.54	259	1.00	0.34	1.02
	10000	239	0.92	0.20	0.59	263	1.01	0.37	1.10
120	2500	256	0.95	0.22	0.66	268	1.00	0.35	1.04
	5000	259	0.96	0.23	0.69	273	1.01	0.36	1.08
	10000	261	0.96	0.24	0.71	276	1.01	0.38	1.10
140	2500	271	0.97	0.26	0.77	280	1.00	0.40	1.17
	5000	271	0.96	0.26	0.76	286	1.02	0.40	1.16
	10000	273	0.96	0.27	0.76	291	1.03	0.45	1.28
180	2500	291	0.98	0.31	0.88	303	1.02	0.54	1.54
	5000	293	0.98	0.33	0.93	313	1.05	0.54	1.54
	10000	298	0.99	0.34	0.95	318	1.06	0.57	1.59
140-LTF	5000	272	0.97	0.26	0.76	295	1.04	0.42	1.23